†Supporting Information 1 (SI1)
Spectroscopic Results for
Improving the Accuracy of Cu(II)-Nitroxide RIDME in the Presence of Orientation Correlation Evaluated in Water-soluble Cu(II)-Nitroxide Rulers

Irina Ritsch,[a‡] Henrik Hintz,[b§] Gunnar Jeschke,[a] Adelheid Godt,[*b] and Maxim Yulikov[*a]

[a] *Laboratory of Physical Chemistry, Department of Chemistry and Applied Bioscience, ETH Zurich, Vladimir-Prelogweg 2, 8093 Zurich, Switzerland.* E-mail: *maxim.yulikov@phys.chem.ethz.ch*

[b] *Faculty of Chemistry and Center for Molecular Materials (CM₂), Bielefeld University, Universitätsstraße 25, 33615 Bielefeld, Germany. E-mail: godt@uni-bielefeld.de*

∗ Corresponding authors

‡ Authors contributed equally. I.R. performed the spectroscopic measurements and data processing. H.H. performed the synthetic work.

Synthesis of the Model Compounds

This document (SI1) contains the Supporting Information for the Spectroscopic Results. The Supporting Information for the Synthesis are to be found in the separate file SI2. For the chemical structures of the rulers refer to Figure 1 in the main text. As in the main text we will refer to [Cu(II)-TAHA]-nitroxide as ruler (or compound) **1**, and to [Cu(II)-PyMTA]-nitroxide as ruler (or compound **2**. In the following we will occasionally abbreviate nitroxide as 'NO'.

List of Solvents

The solvents that were used to dilute the model compounds from the stock solution were: H_2O deionised in house on a MiliPore Synergy water purification system (Merck), D_2O (Sigma-Aldrich, 99.8 atom % D, Lot: STBF4512V), glycerol$-d8$ (Sigma-Aldrich, >98 atom % D, >98% , Lot: MBBC0482) and glycerol (Acros Organics, 99%, Lot: 1691854).

EPR Characterisation of Model Compounds

The EPR spectra of the Cu(II) and nitroxide components of the rulers **1** and **2** were measured at X-band (continuous wave (CW), 140 K) and Q-band (echo-detected EPR (EDEPR), 20-50 K). All CW experiments were performed on a commercial Bruker Elexsys spectrometer with a liquid nitrogen cryostat in the Bruker SHQ resonator. Unless stated otherwise, all pulsed Q-band experiments were performed on a commercial Bruker E580 X/Q spectrometer upgraded to a high MW power,[1] equipped with a home-built resonator for large-diameter samples.[2]

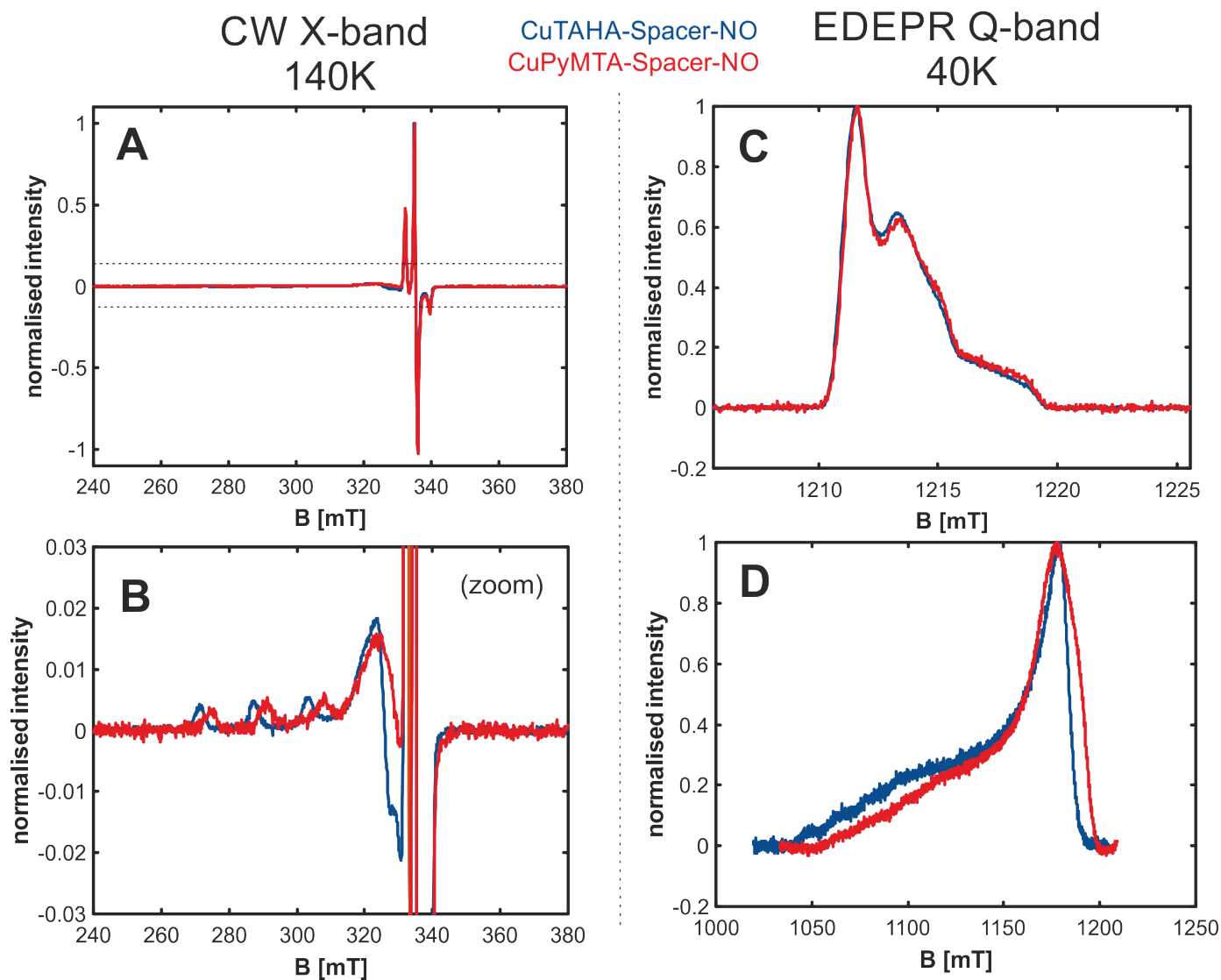### EPR Spectra of the Rulers 1 and 2

For the X-band measurements (SI1 Figure 1A and B) both rulers **1** and **2** were diluted to 400 μM in D_2O/H-glycerol (1:1 %V) solvent, for the Q-band measurements (SI1 Figure 1C and D) the concentration was 100 μM in fully deuterated solvent (1:1 %V D_2O/d_8-glycerol). 40 μl (X-band) resp. 35 μl (Q-band) of sample were transferred to a 3 mm (outer diameter) quartz capillary and frozen by immersion in liquid nitrogen. The CW X-band spectra were measured with 30 dB MW attenuation for the Cu(II) component sub-spectra, and 48 dB attenuation for the zoom-in on the nitroxide component (not shown), which in both cases avoided saturation. The EDEPR spectra at Q-band were measured with a refocusing delay of $\tau = 400$ ns, using an appropriate shot repetition rate (*srt*) for the given spin type and temperature. At both MW frequencies the nitroxide spectra of the two rulers are very similar to each other, whereas the Cu(II) components clearly differ. The spectrum of [Cu(II)-TAHA] in ruler **1** is slightly shifted towards higher g-values than that of [Cu(II)-PyMTA] in ruler **2**. In the spectrum of [Cu(II)-TAHA] the four ^{14}N hyperfine lines for the axial (z) orientations are clearly resolved, while they are broadened in [Cu(II)-TAHA]. The nitroxide component of EDEPR Q-band spectrum of the ruler **1** at 30 K was fitted with the EasySpin[3] '*pepper*' function ($S = 1/2$ coupled to one ^{14}N spin with $I = 1$). The final fit parameters are $\{g_x, g_y, g_z\} = \{2.0120, 2.0106, 2.0060\}$, $\{A_x, A_y, A_z\} = \{24.20, 24.03, 96.30\}$ MHz, and $lwpp = 0.6968$. This fit was used to generate the inset of Figure 2A in the main text.

NO-NO DEER as a control experiment for aggregation in the model compound samples

To check that the rulers are homogeneously distributed in the sample tube we performed NO-NO Double Electron-Electron Resonance (DEER) at standard conditions (50 K, $t_1 = 400$ ns, $t_2 = 4000$ ns, all pulse lengths 12 ns, averaged over ~12 h) (SI1 Figure 2).[1] If aggregation were relevant in the samples, we would expect a deviation of the signal from an exponential background decay function, or even visible inter-molecular dipolar contributions in the form factor. In the case of [Cu(II)-TAHA]-nitroxide **1** there some oscillation are very faintly visible, but the modulation depth of this potential signal is extremely low ($< 2\%$). The absence of a strong signal in this experiment, and the excellent fit of the background function with a standard 3-dimensional background model confirms the monomeric state of the molecules and thus excellent solubility in aqueous solvents as expected from the PEGylated rulers. The experiments were performed at a ruler concentration of 200 μM.

Relaxation measurements

Longitudinal relaxation of both spin types in ruler **1** was measured by the Inversion Recovery experiment ($\pi - t - \pi/2 - \tau - \pi - \tau$−det). Transverse relaxation was then measured with an appropriate *srt* by a Hahn echo decay ($\pi/2 - \tau - \pi - \tau$−det) . The same sample tubes as for the RIDME modulation depth optimisation and the Q-band EDEPR measurement were used. Experiments in this series were recorded at the maxima of the respective spectra using 12/24 ns (for $\pi/2/\pi$) pulses on the stripline channels of the commercial spectrometer. While this corresponds to a relatively hard pulse in the case of nitroxide, it is still a comparatively soft pulse for detection in the much broader spectra of the Cu(II) complexes. The curves and fits using three different models (mono-exponential, bi-exponential, and stretched exponential) are shown in SI-Figure 3, resp. SI-Figure 4 for [Cu(II)-TAHA]-nitroxide **1** and in SI-Figure 5, resp. SI-Figure 6 for [Cu(II)-PyMTA]-nitroxide **2**. Longitudinal relaxation of the Cu(II) spins is orders of magnitude faster than longitudinal relaxation of the nitroxide spins at all considered temperatures. Transverse relaxation is similar for the two spin species, but typically slightly slower for the nitroxides. A mono-exponential fit to the transverse relaxation curves is typically not a good approximation for nitroxides below

SI1 Fig. 1 X-band cw spectra and Q-band EDEPR spectra of rulers **1** (blue) and **2** (red) normalised to the maximum of each spectrum; the spectra are slightly shifted along the B-axis to account for slightly different experimental microwave-frequencies. (A) Full range of the CW experiment at 140 K recorded with a modulation amplitude of 4 G at 30 dB microwave attenuation; the nitroxide components of the the two spectra slightly saturates at this microwave power, which is relevant when fitting is attempted. (B) vertical zoom on Cu(II) components as indicated by dashed line in (A); the $g_{zz}^{(Cu)}$-value of ruler **1** appears to be higher than that of ruler **2**. (C) Q-band EDEPR spectra in the nitroxide range at 40 K; the spectra are almost identical for the two rulers. (D) Q-band EDEPR spectra in the Cu(II) range at 40 K; the hyperfine splitting in the low-field range (z-orientations) is better resolved for ruler **1**.
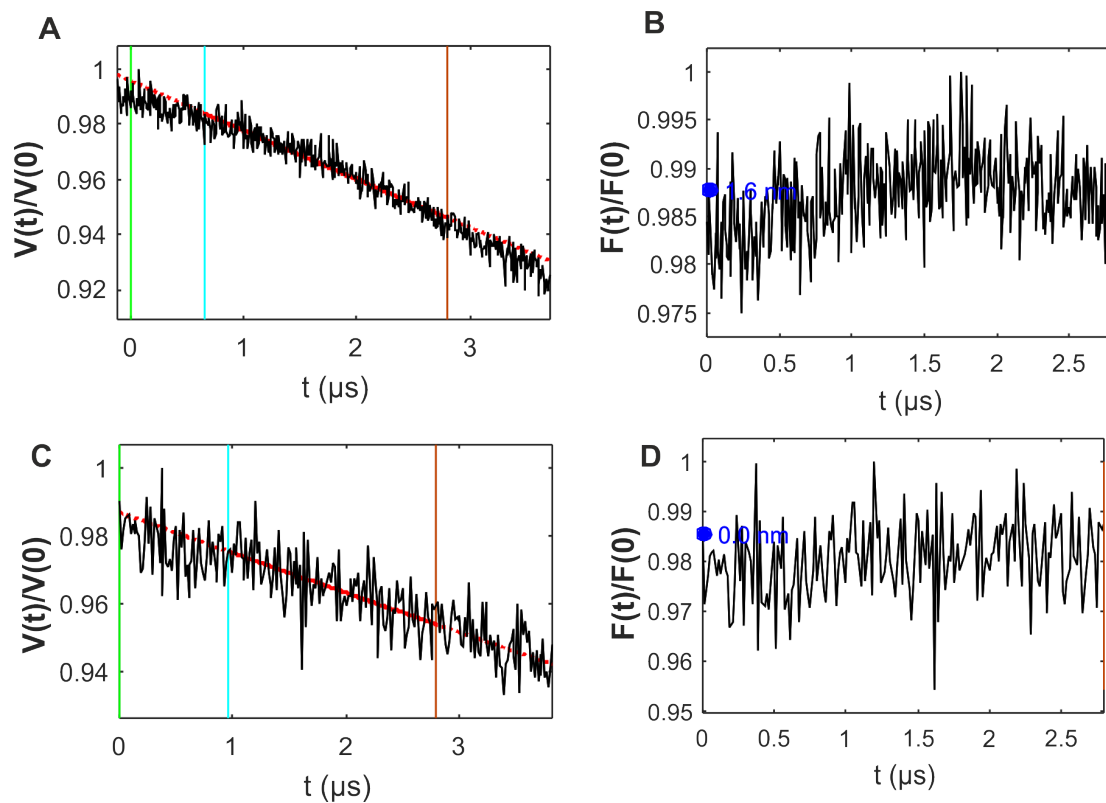
SI1 Fig. 2 NO-NO 4p-DEER at 50 K on the model compounds with standard settings: all 12 ns pulses, pump on maximum of nitroxide, detection 100 MHz below, acquisition time ≈12 h; (A-B) primary data, resp. form factor for [Cu(II)-TAHA]-nitroxide **1**; (C-D) primary data, resp. form factor for [Cu(II)-PyMTA]-nitroxide **2**; for both rulers we find only background contribution to the dipolar time traces, which can be fitted with an exponential function.

SI1 Tab. 1 Relaxation properties of ruler 1 (left) and ruler 2 (right); this is an extension of Table 1 in the main text. Here we report the time until the signal has relaxed towards ≈ 87 %, resp. 63 % and ≈ 87 %, of the equilibrium intensity for inversion recovery, resp. 37 % and 14 % of the initial intensity for transverse relaxation. These levels are indicated by the dashed lines in SI1 Figures 3-6(C) and (G). The larger the difference between the first and the second recovery time, the more the behaviour deviates from a mono-exponential decay.

ruler 1	10 K	20 K	30 K	40 K	50 K	ruler 2	10 K	20 K	30 K	40 K	50 K
signal recovered to	IR NO [ms]					signal recovered to	IR NO [ms]				
$1-1/e^2 \approx 0.87$	63.9	8.5	2.6	1.1	0.8	$1-1/e^2 \approx 0.87$				1	
$1-1/e \approx 0.63$	31.3	4.3	1.3	0.5	0.4	$1-1/e \approx 0.63$				0.5	
	IR Cu(II) (maximum) [µs]						IR Cu(II) (maximum) [µs]				
$1-1/e^2$	3881	120	17	6	3	$1-1/e^2$			13	5	
$1-1/e$	2022	57	18	2	1	$1-1/e$			5	2	
signal decayed to	Tm NO [µs]					signal decayed to	Tm NO [µs]				
$1/e \approx 0.37$	8.7	9.1	7.3	4.4	3.2	$1/e \approx 0.37$			7.3	4.3	
$1/e^2 \approx 0.14$	3.7	4.1	3.4	3.5	3.5	$1/e^2 \approx 0.14$			3.9	3.5	
	Tm Cu(II) (maximum) [µs]						Tm Cu(II) (maximum) [µs]				
$1/e$	7.7	6.7	4.2	2.4	1.7	$1/e$				2.2	
$1/e^2$	3.6	3.6	2.7	1.5	0.8	$1/e^2$				1.4	

40 K. The relaxation properties are summarised in SI-Table 1. The relaxation properties of the nitroxides in rulers 1 and 2 are very similar under the tested conditions. Longitudinal relaxation of the Cu(II) spins in [Cu(II)-PyMTA]-nitroxide 2 is slightly slower.

Orientation-Dependent Relaxation Measurements for Cu(II)

As is pointed out in the main text we can assume to average the RIDME contributions from all orientations of the Cu(II) spins in nitroxide-detected RIDME as long as the mixing time exceeds the characteristic longitudinal relaxation time of all possible orientations of Cu(II). In SI1 Figure 7 we demonstrate that, while there are differences in longitudinal relaxation at different positions in the Cu(II) spectrum, these are small compared to the mixing times that can be used in nitroxide-detected RIDME. This is both the case for Cu(II) in model compound 1, and Cu(II) in the same ligand environment, but not covalently linked to the nitroxide-spacer moiety (compound 20).

Saturation of Nitroxide Spins at Low Temperatures and short *srt*

We performed control experiments to ensure that measuring nitroxide-detected RIDME with slight saturation of the nitroxide spins (i.e. too short *srt*) does not introduce artefacts. This is demonstrated for two experimental conditions in SI1 Figure 10.

Theoretical description of orientation averaging in PDS experiments

Orientation selection in dipolar EPR spectroscopy has been studied extensively for more than a decade.[4–17] Here we focus on the problem of reliably obtaining the distance distribution in the presence of orientation correlation. We first treat the general case, where spectral selection occurs for both A and B spins and we consider the form factor that results after correcting for the intermolecular background decay, up to an additive constant that may arise from partially spin-labelled molecules.

We start with defining the excitation profile corresponding to the action of all pulses applied at the detection frequency. For the four-pulse DEER experiment this would correspond to a sequence, consisting of one $\pi/2$ pulse and two π pulses, the so-called refocused Hahn echo sequence. In the case of the RIDME pulse sequence, shown in Fig. 2(A), we have to consider the cumulative effect of all five pulses, in order to define the frequency profile of the spin packet responsible for the so-called refocused virtual echo (RVE).[18] Let's abbreviate the excitation probability of the detection part of the pulse sequence as $P_d(\omega)$. In analogy to this, we can define the inversion probability $P_{inv}(\omega)$ which would describe either the excitation profile of the pump pulse in the DEER experiment, or the spin flip probability for the B spins during the RIDME mixing block.

We neglect the excitation of detected spins (A spins) by the part of the pulse EPR experiment responsible for the inversion of the partner spins (B spins). Note that, depending on the PDS experiment, the inverting part of the pulse sequence can be a microwave pulse, a collection of such pulses, or a longitudinal spin-flipping mixing block, as in the RIDME experiment. For PDS experiments, involving one of these forms of B-spin inversion, this assumption is equivalent to neglecting the overlap of the pump and the detection excitation profiles. For nitroxide-based or metal ion-based spin labels and DEER or RIDME experiments, this assumption is in most cases a reasonable approximation, but it is not suitable for paramagnetic species with very narrow EPR spectra (such as trityl radicals), and single frequency experiments of the type of DQC or SIFTER.[19,20]

Geometry of an arbitrary spin pair consisting of one A spin and one B spin is fully described by five angles and one distance. For characterising this geometry, one usually chooses the three Euler angles (α, β, γ) that relate the molecular frame of the B spin to the one

of the A spin and the two polar angles (θ_{dd}, ϕ_{dd}) that specify the direction of the spin-spin vector in the A spin molecular frame. For the orientation averaging problem, it is more convenient to consider the orientations of the static magnetic field $\vec{B}_0$ in the two molecular frames and the angle between the magnetic field and the spin-spin vector. The orientation of $\vec{B}_0$ in the eigenframe of the g tensor of the A spin is uniquely defined by the angles θ_A and ϕ_A. We will loosely refer to this pair of angles as to the orientation of the A label with respect to the static magnetic field. Regarding orientation, the resonance frequency or field of the A spin depends on only these two angles, since the hyperfine tensors have a fixed orientation with respect to the g tensor, but it also depends on the nuclear spin states of the surrounding nuclei. For nitroxide radicals it is sufficient to consider only the hyperfine coupling to the nitrogen nucleus, since the hyperfine interactions with protons are weak and combine to a nearly isotropic broadening. For Cu(II) centres, it is usually sufficient to only consider the hyperfine interaction with the ^{63}Cu or the ^{65}Cu nucleus. We can thus write the resonance frequency of the A spins as $\omega_{A,k}(\theta_A, \phi_A)$, with the index k indicating the corresponding nuclear spin state. Analogously, for the B spin we can write the EPR frequency as a function of the two eigenframe angles and the corresponding nuclear spin state: $\omega_{B,j}(\theta_B, \phi_B)$. Finally, we define θ as the angle between the spin-spin vector and the static magnetic field.

If we consider an ideal frozen glassy solution sample, the individual probability distribution for the angle pairs θ_A, ϕ_A and θ_B, ϕ_B are isotropic, as is the one of θ. In the case of (semi-)rigid molecules, however, we cannot assume that the two angle pair distributions are uncorrelated with each other and with the distribution of θ. Let's then describe the orientation of the B spin by a conditional probability distribution $P(\theta_B, \phi_B|\theta_A, \phi_A)$, which denotes the chance to find the specified orientation of the B spin, for a given orientation of the A spin. Next, we need to define the conditional probability $P(\theta|\theta_A, \phi_A; \theta_B, \phi_B)$ to find the given dipolar angle θ for the given fixed angle pairs θ_A, ϕ_A and θ_B, ϕ_B. These distributions are assumed to be averaged over all nuclear spin states. We assume the following normalisation for the two conditional probabilities:

$$\int_0^{2\pi}\int_0^{\pi} P(\theta_B, \phi_B|\theta_A, \phi_A) \sin\theta_B d\theta_B d\phi_B = 1, \tag{1}$$

and

$$2\pi \int_0^{\pi} P(\theta|\theta_A, \phi_A; \theta_B, \phi_B) \sin\theta d\theta = 1. \tag{2}$$

Equation (1) implies that for any orientation of the A spin there exists a B spin, which has some orientation with respect to the external magnetic field (i.e. we consider only doubly labelled molecules). The distribution of such possible B-spin orientations is generally not isotropic. Equation (2) is a simple statement that for all allowed orientations of the A and the B spins there is one or more possible orientations of the spin-spin vector with respect to the external magnetic field. This equation also implies the obvious fact that, when we pass through all θ angles, we sample all possible orientations of the spin-spin vector.

By integrating the product of these two conditional probabilities over the angles θ_B, ϕ_B, we obtain the conditional probability for the dipolar angle θ given the A spin orientation is θ_A, ϕ_A:

$$\int_0^{2\pi}\int_0^{\pi} P(\theta_B, \phi_B|\theta_A, \phi_A)P(\theta|\theta_A, \phi_A; \theta_B, \phi_B) \sin\theta_B d\theta_B d\phi_B$$

$$= P(\theta|\theta_A, \phi_A). \tag{3}$$

This probability relates the resonance frequencies of an A spin hyperfine multiplet, fully specified by θ_A, ϕ_A to the distribution of dipolar frequencies that depends on distance r and on the distribution of θ. We note in passing that for distributed distances and spin pair geometries all probabilities depend on r if the distribution of r is correlated to the distribution of α, β, γ, θ_{dd}, and ϕ_{dd}.

If we now integrate $P(\theta|\theta_A, \phi_A)$ over the isotropic distribution of the θ_A, ϕ_A angles ($P(\theta_A, \phi_A) = 1/4\pi$), we must obtain an isotropic distribution for the dipolar angle:

$$\int_0^{2\pi}\int_0^{\pi} P(\theta_A, \phi_A)P(\theta|\theta_A, \phi_A) \sin\theta_A d\theta_A d\phi_A = P(\theta) = \frac{1}{4\pi}. \tag{4}$$

This description can be conveniently related to the situation in PDS experiments by including the excitation profiles of the two spins $P_d(\omega_A)$ and $P_{inv}(\omega_B)$. Including summation over the two sets of nuclear spin states, we then obtain the equation for the dipolar time evolution signal in the form

$$V(r, \theta, t) = \sum_{k,k'} \int_0^{2\pi}\int_0^{\pi} \left[\int_0^{2\pi}\int_0^{\pi} P(\theta_B, \phi_B|\theta_A, \phi_A)P(\theta|\theta_A, \phi_A; \theta_B, \phi_B) \right.$$

$$\times P_d(\omega_{A,k}(\theta_A,\phi_A))P_{inv}(\omega_{B,k'}(\theta_B,\phi_B))$$

$$\times \cos[\omega_d(r,\theta)t]\sin\theta_B d\theta_B d\phi_B \Bigg] \sin\theta_A d\theta_A d\phi_A. \tag{5}$$

Here, $V(r,\theta,t)$ is the contribution to the time evolution signal from the molecules with dipolar angle θ. For simplicity, we consider only the case where all molecules have the same spin-spin distance r. A distance distribution with a width comparable to the mean distance can be treated by additional weighted integration over r. For any individual spin-spin distance, the full dipolar evolution signal can be obtained just by the integration over the dipolar angle θ

$$V(r,t) = 2\pi \int_0^\pi V(r,\theta,t)\sin\theta d\theta. \tag{6}$$

We note that Equation (5) simplifies considerably if $P_{inv}(\omega_{B,k'}(\theta_B,\phi_B))$ is uniformly distributed, i.e., in the case where the probability of B spin inversion does not depend on orientation of the B label. We then have

$$V(r,\theta,t) = P_{inv} \sum_{k,k'} \int_0^{2\pi}\int_0^\pi P(\theta|\theta_A,\phi_A)P_d(\omega_{A,k}(\theta_A,\phi_A))$$

$$\times \cos[\omega_d(r,\theta)t]\sin\theta_A d\theta_A d\phi_A. \tag{7}$$

The aim of an orientation averaging procedure would be to set up one or several dipolar evolution measurements in such a way that the sum of all excitation profile products $P_d P_{inv}$ approaches a uniform distribution over ω_A and ω_B. If this is the case, using equations (3)-(4), we arrive at the simple formula

$$V_{iso}(r,t) = \frac{1}{2} \int_0^\pi \cos[\omega_d(r,\theta)t]\sin\theta d\theta. \tag{8}$$

If P_{inv} is uniformly distributed, such an isotropic signal can be obtained by adding data sets from experiments that together provide a uniform distribution P_d. This is a tremendous simplification, since an excitation scheme with uniform sum of all P_d can be constructed easily and without knowing the geometry of the system. In contrast, an excitation scheme, where the sum of all $P_d P_{inv}$ is uniform, is difficult to design and such design does require knowledge of system geometry.

Equation (8) corresponds to the isotropic distribution of dipolar angles, and is represented in the dipolar frequency domain by the well-known Pake pattern for a fixed spin-spin distance r. This is the kernel function for the majority of programs available for analysing dipolar evolution EPR data. The ultimate goal of any orientation averaging is to arrive at the best possible approximation of this function, in order to remove the angles from consideration, and have an opportunity to restrict the analysis solely to the spin-spin distance distribution.

In the following, we discuss possible approaches to obtain such orientation-averaged dipolar evolution data. As the first approach, one can perform conventional DEER experiments with different pump and detection positions within the EPR spectra of A and B spins, and add these time evolution data.[21] If we assume complete spin labelling, then the electron spin echo intensity is a measure of the fraction of excited A spins, i.e. it corresponds to the probability $P(\theta_A,\phi_A)$ integrated over the excitation profile of the detection subsequence. Otherwise, the labelling efficiency f_A of the A spins enters as an additional factor. The relative depth of the dipolar oscillation corresponds to the conditional probability of inverting the B spins coupled to the observed A spins. For incomplete labelling, this depth is multiplied by the labelling efficiency f_B of the B spins. The integration in the equation (5) corresponds, thus, to a summation of dipolar evolution traces over a series of DEER experiments, so that each trace is taken with the weight, according to the detected echo amplitude. For a series of DEER experiments, this means summation according to the EPR echo amplitudes at the given resonance positions.

For the DEER experiment, where detection and pump pulses are applied at two different frequencies, this scheme potentially allows combining nearly any resonance frequencies for A and B spins. There are, however, a few problems related to this approach.

Problem 1: Microwave pulses with rectangular time profiles do not have rectangular profiles in the frequency domain. Furthermore, these frequency profiles contain side bands, which overlap with the excitation profiles of the pulses at the neighbouring pump/detection positions. Note that the microwave pulses must not be made too 'soft', i.e. narrow-banded, since they have to cover the entire dipolar spectrum of the A-B spin pairs. Nonetheless even a carefully measured and summed set of the conventional DEER data likely contains 'peaks' and 'dips' in the cumulative excitation profile $P_d(\omega)$ and $P_{inv}(\omega)$.

Problem 2: In cases where the EPR spectra of A and B spins (partially) overlap the resonance frequencies of the two spins are the same for some combinations of A and B spin orientations. The DEER experiment cannot detect dipolar evolution data for such cases, thus averaging of A and B spin orientations is not complete, even for a full set of DEER traces detected at all practically accessible pairs of resonance positions (ω_A, ω_B). Single-frequency experiments (for example DQC, SIFTER) provide a signal from pairs with nearly identical resonance frequencies. Note however, that detection bandwidth of such experiments often cannot cover the total spectra width of the A and B spins, which again excludes complete averaging.

Problem 3: For cases where the resonance frequency difference between A and B spins is comparable to the dipolar frequency, the pseudo-secular terms in the dipole-dipole interaction operators mix electron spin states of the A-B pairs and thus the dipolar spectra are distorted. This problem is of less importance for paramagnetic species with broad EPR spectra, where the fraction of A-B spin orientations corresponding to this problematic case is small. This, however, can become an issue for radicals with narrow EPR spectra, for instance trityls. This problem cannot be solved by applying a different PDS technique.

Problem 4: If the EPR spectra of one or both types of paramagnetic species are broad, then setting up DEER measurements for all possible combinations of detection and pump frequencies becomes difficult, due to resonator bandwidth limitations and, eventually, also due to bandwidth limitations of the microwave bridge components. A similar problem appears, if the spectra of A and B spins do not overlap, and the gap between the spectra is of the order of the bandwidth or larger. Here we present such an example for the Cu(II)-nitroxide case.

Note that not in all cases when the problems 1-3 are present, they lead to significant problems in the orientation averaging schemes. Due to the partial flexibility of the ruler molecules, the distributions of the *g*- and hyperfine tensor parameters, and overlap of different hyperfine components in the EPR spectra of the Cu(II) and nitroxide spin labels, very often the formally improper orientation averaging protocols work pretty well and allow obtaining sufficiently accurate orientation-averaged PDS data. It is important, however, to keep in mind that all mentioned problems are based on the fundamental equations, and thus they are always present and affect the averaged PDS data to some extent. Thus, it is important to understand their origin and to define procedures to reduce these problems if they appear in practical work.

The use of broad-band shaped pulses considerably alleviates Problem 1, since better control of the pulse excitation profiles is available. In frequency domain the central regions of the excitation profiles can be made reasonably flat, side bands can be strongly suppressed and the edges can be made steeper than for non-shaped rectangular pulses.[22,23] This significantly reduces the number of necessary pump-detection frequency combinations compared to the case of non-shaped rectangular pulses, and a better approximation of the isotropic excitation profiles, P_d and P_{inv}, can be achieved. Broad-band modifications of some existing conventional PDS experiments have been developed based on these improvements.[24–26] Thus, a second approach for orientation averaging is based on broadband microwave pulses.

Problem 2 can be addressed by the use of single-frequency experiments with broadband excitation, whereas no simple averaging procedure can address problem 3. This is because the pseudo-secular part of the dipole-dipole interaction entangles the dipole-dipole coupling with the difference of the resonance frequencies of the A and B spins and thus with orientation correlations in a way that cannot be separated by a PDS experiment. If problem 3 is significant, accurate distance analysis requires that system geometry is elucidated. Note, however, that the problem simplifies again if the sum of dipole-dipole coupling and exchange coupling is much larger than the difference of resonance frequencies at all orientations. In this regime, PDS experiments provide a Pake pattern that is 1.5 times as broad as the one in the weak-coupling case and does not depend on exchange coupling or relative orientation.[27]

Problem 4 can be partially addressed by a combination of broadband excitation with dedicated broadband[28] or bimodal[29] EPR resonators. The variations of the resonance frequencies in different spin label pairs can be, however, so large that even at the best currently available setups only partial orientation averaging can be achieved.

The use of the RIDME mixing block solves the problem of the large resonance frequency offset for the pumped spins. Orientation dependence persists only in the case of a strong anisotropy of the longitudinal relaxation of the B spins, which makes the effective profile of B spin inversion non-uniform at short and moderate mixing times. The case of long mixing times will be discussed below. However, the conventional RIDME experiment still requires summing dipolar evolution data for several detection positions. In this work we demonstrate that a broadband detection sub-sequence can address this problem.

The Cu(II)-nitroxide system is a good test case for these considerations, since the Cu(II) spectrum is usually too broad for excitation with even ultra-wideband technology, and, at the same time, the nitroxide EPR spectrum is too broad for full excitation by rectangular pulses, but can be fully and uniformly excited by broadband pulses that have been shown to cover a bandwidth up to 800 MHz.[30]

Data processing in DeerAnalysis

All data were processed using the DeerAnalyis2016 software (www.epr.ethz.ch\software.html). An example is given in SI1 Figure 8, where we demonstrate that our standard choice of t_2 in all RIDME traces is sufficiently long to accurately predict shape and position of the distance distribution of ruler **1**.

g-Factor correction of the dipolar coupling frequency

The correction of the dipolar coupling frequency can be approximated by

$$\omega_{\perp,\mathrm{eff}}(r) = \frac{g_B}{g_e} \frac{52.04\,\mathrm{MHz}}{(r/1\,\mathrm{nm})^3} \tag{9}$$

Even though the effect is typically small, it may become relevant when simulating and fitting orientation-selective RIDME traces. Note also that in case of strong *g*-anisotropy, if the preferred spin-spin vector orientation is fixed with respect to the *g*-tensor eigenframe, then even accurately orientation averaged dipolar spectra would still contain information on this orientation. For instance, if the ratio of the dipolar frequency in the parallel and in the perpendicular orientation is larger than two, then parallel orientation of the spin-spin vector correlates with higher *g*-value orientations, and the perpendicular orientation of the spin-spin vector correlates with the smaller *g*-value orientations of the *g*-eigenframe.

Dipolar Spectrum for Cu(II)-detected UWB-DEER

The fit of the form factor, and the dipolar spectrum of the UWB-DEER measurement presented in Figure 12 in the main text are shown in SI1 Figure 11.

ESEEM averaging cycles and alternative ESEEM suppression

The individual traces of an ESEEM averaging cycle with $d_{\mathrm{ES}} = 16\,\mathrm{ns}$ are shown in SI1 Figure 9(B). In Panel (C) we show more examples of ESEEM suppression by using a long t_1. Note that ^{2}H-ESEEM arising from solvent molecules presents a rather fortunate case: while a lower degree of solvent deuteration typically leads to faster transverse relaxation and thus puts a limit on the maximum t_1 that can be used, it also automatically implies a lower amplitude of the ^{2}H-ESEEM modulation, which can tolerate less efficient suppression. This may not apply to nuclei that belong to the spin label. Further prolongation of t_1 may still help in severe cases of ESEEM, but it may be sufficient (and better in terms of sensitivity) to remove the remaining ^{2}H-ESEEM contamination by t_1 and t_2 averaging. A coarse-grained screening for experimental settings supporting this proposed choice of parameters is given in SI1 Figures 12 and 13.

Additional Results for Sensitivity Analysis

Optimisation of mixing time and temperature

This sections explains the considerations for the optimisation of temperature and mixing time. For clarity the optimisation is split into a factor $D_{r_{\mathrm{max}}}(T, T_{\mathrm{mix}})$ summarising the signal losses from relaxation of the detected spins, and an empirical factor $\lambda(T, T_{\mathrm{mix}})$, which reflects the buildup of modulation depth. The subscript indicates that the final sensitivity optimisation depends on the distance to be measured and should be evaluated for an (approximate) longest distance r_{max}. All characteristic relaxation times used as parameters in the following depend on temperature. For the part that parametrises the relaxation of the detected spins we use

$$D_{r_{\mathrm{max}}} = \exp(-T_{\mathrm{mix}}/T_{3p,\mathrm{NO}} - 2\,t_{r_{\mathrm{max}}}/T_{m,\mathrm{NO}}) \cdot \sqrt{T_{\mathrm{ref}}/T_{1,\mathrm{NO}}}, \tag{10}$$

where $T_{m,\mathrm{NO}}$ and $T_{1,\mathrm{NO}}$ are the transverse and longitudinal relaxation times of the nitroxide spin, respectively. $T_{3p,\mathrm{NO}}$ is the characteristic echo decay time that would be observed when increasing the second inter-pulse delay of a 3-pulse ESEEM experiment. This parameter is an addition to the treatment in Jeschke and Polyhach[31] and it takes into account that the nitroxide spins relax during the mixing time. Typically it is a very good approximation that $T_{3p,\mathrm{NO}} \approx T_{1,\mathrm{NO}}$, which is also what we use in all further calculations below.

Transverse relaxation acts during the transverse evolution time $t_{r_{\mathrm{max}}}$ and we assume a mono-exponential decay of the echo intensity during this interval. This may not be a very good approximation for nitroxides below 30 K (compare SI1 Figures 4 and 6), but we did not investigate more complex relaxation models in this context. Note that the required trace length $t_{r_{\mathrm{max}}}$ of a PDS experiment in order to observe at least one full period of the dipolar oscillation arising from a distance r_{max} can be calculated from the well known relation $t_{r_{\mathrm{max}}} = 1 \cdot (r_{\mathrm{max}}/\mathrm{nm})^3/52.04\,\mathrm{MHz}$ (inversion of Equation (9)). The factor $\sqrt{T_{\mathrm{ref}}/T_{1,\mathrm{NO}}}$ accounts for the fact that at lower temperatures it is necessary to use lower shot repetition rates to avoid saturation of the detected spin, and T_{ref} is an arbitrary reference time to obtain a dimensionless parameter.

For the second part of the optimisation, which relates to the buildup of modulation depth we use

$$\lambda(T, T_{\mathrm{mix}}) = \lambda_{\mathrm{max}}(T) \cdot 2\,P_{\mathrm{odd}}(T_{\mathrm{mix}}) \tag{11}$$

$$= \lambda_{\mathrm{max}}(T) \cdot \left(1 - \exp(-T_{1,\mathrm{Cu}}/T_{\mathrm{mix}})\right). \tag{12}$$

This includes the buildup kinetics following P_{odd} given by Equation (13) in the main text and empirically introduces the experimentally observed plateau values for λ as the parameter $\lambda_{\mathrm{max}}(T)$. For $\lambda_{\mathrm{max}}(T)$ we use here the experimentally determined maximum modulation depths as shown and tabulated in the main text.

Combining the two factors we arrive at the quantity

$$S_{r_{\max}}(T) = \frac{1}{T} \cdot D_{r_{\max}}(T, T_{\mathrm{mix}}) \cdot \lambda(T, T_{\mathrm{mix}}) \tag{13}$$

$$\approx \frac{1}{T} \cdot \exp(-5\, T_{1,\mathrm{Cu}}/T_{1,\mathrm{NO}}) \cdot \exp(-2\, t_{r_{\max}}/T_{m,\mathrm{NO}})$$

$$\cdot \sqrt{T_{\mathrm{ref}}/T_{1,\mathrm{NO}}} \cdot \lambda_{\max}(T) \tag{14}$$

which also includes a weighting by $1/T$ to account for the temperature dependence of spin polarisation of the detected spin (following Boltzmann statistics in the high temperature approximation). This equation is also given in the main text.

Solvent Deuteration

Solvent deuteration has a strong influence on the background decay. This may shift the optimal choice of T_{mix}, which was not further investigated in this study, but is demonstrated in SI1 Figure 19(A). In SI1 Figure 19(B) we show an example of the modulation depth artefact induced by an echo-crossing.

Additional Figures for Modulation Depth Build-Up for[Cu(II)-TAHA]-nitroxide 1

In SI1 Figure 20 we show the data that were used to extract the modulation depths reported in Figure 6 in the main text.

Modulation Depth Build-Up for [Cu(II)-PyMTA]-nitroxide 2

In SI1 Figure 21 the modulation depth build-up for one temperature is shown for ruler **2**. As for ruler **1** a stable plateau is reached. The longitudinal relaxation time of Cu(II) in this system at this temperature is $T_{1,\mathrm{Cu}} = 13\,\mu s$, we therefore empirically expect to reach the modulation depth plateau at $T_{\mathrm{mix}} = 5 \cdot 13\,\mu s = 65\,\mu s$. Experimentally we observe the beginning of the plateau region between $T_{\mathrm{mix}} = 50\,\mu s$ and $T_{\mathrm{mix}} = 100\,\mu s$, which thus is in excellent agreement. Note that in this case an even longer $t_1 = 6.1\,\mu s$ was necessary to suppress the background artefact.

Background Fitting

We found that the stretched exponential fit of the RIDME background (BG) is often not a good model for nitroxide-detected RIDME. This we observed not only for our model compounds, but also on reference samples. In SI1 Figure 12 we show RIDME background measurements on a mixture of tempol with [Cu(II)-TAHA] (compound **20**) in fully deuterated solvent at different temperatures and varying T_{mix}. Along the vertical axis we increased the length of the first refocusing delay t_1, while keeping t_2 fixed. The dashed lines are a guide to the eye for a 'ridge'-like feature in the background shape that leads to a deviation from the stretched exponential decay. This feature is present in a large range of conditions, and moves with t_1, until it disappears after $t_1 \approx t_2$ in this case. This may be a coincidence for this particular choice of t_2. Note, that ESEEM modulations generally are strongly suppressed when increasing t_1.

The same artefact is observed in samples of only tempol (SI1 Figure 13). Here we measured a series with different solvent compositions with varying mixtures of D_2O and H_2O. The percentage of H_2O written in the figure is given as the volume fraction of total sample volume. In each vertically shifted trace we increased t_1. The experimental temperature of 50 K is not optimal for nitroxide-detected RIDME, but was chosen for technical reasons: Sample exchange was performed at 80 K, to reduce the danger of freezing the movable parts of the resonator by ice formed from air contaminations. Thus, flashing the resonator to 80 K and the following probe-head and sample equilibration at the measurement temperature were more efficient if RIDME measurements were performed at 50 K. We observed that with higher degree of protonation, it is still possible (even if more challenging) to find a choice of t_1 where the background is well approximated by a single stretched exponential while maintaining a reasonable SNR (which decreases due to transverse relaxation with longer t_1). Although more rigorous testing is required to understand this background issue, we observed that the t_1 required to obtain a stretched exponential-type background shape coincides with the time t, after which the 3p-echo decay $(\pi/2 - t - \pi - 2\tau - \pi - \tau - \det)$ is a monotonously decaying function. For this particular sample this happens at $\approx 4\,\mu s$ (see SI1 Figure 14). The background fitting with a stretched exponential is empirically found to be much more stable with respect to the fitting range when a sufficiently long $t1$ is used, as is demonstrated in SI1 Figure 15. We observed that in RIDME time-evolution during t_1 and t_2 is not strictly equivalent. Even just using $t_1 > t_2$ with a constant t_{max} can slightly suppress the unwanted background shape at early times in the trace (compare dark purple, and dark blue trace in SI1 Figure 16). The background fit and extracted modulation depth no longer vary after a critical t_1 has been surpassed.

As is discussed in the main text, we evaluated the frequency-domain signature of the RIDME background function in situations where we observed deviations from the stretched background model. The data from the reference sample are presented in SI1 Figure 17A, where the frequency-domain plot is the same as in the main text in Figure 5. The stretched exponential model is clearly unsuitable in this case. A much better result can be achieved with a bi-exponential fit. In the background corrected data (red curves) we still observe

a slowly oscillating component which is consistent with the ESEEM frequencies expected for ^{14}N at Q-band. A similar background shape was observed for a sample of Maleimido-Trityl (abbreviated here as MTrt, 50 μM, deuterated solvent, detected at 80 K) (see SI1 Figure 17(B)). In this case the proposed ^{14}N ESEEM contribution is not observed as expected.

We have pointed out in the main text that the background artefact is not a severe problem for the extraction of distance distributions that are very narrow (as for example ruler **1**), because the dipolar oscillations in such cases are well resolved, yielding a stable fit. For dipolar traces where no distinct oscillations can be observed, such as for ruler **2**, (which could be due to a broad underlying distance distribution, or a distribution of exchange couplings) the problem is much more severe. In SI-Figure 18(A) we show that an incorrect fit of the background function leads to a strong artefact peak in the distance distribution at ≈ 2.8 nm. This peak is suppressed when using an appropriate t_1, as is demonstrated in SI-Figure 18 (same figure as Figure 10 in main text). In both cases we attribute the additional intensity in the low distance range (1.5-2.2 nm) as artefacts due to significant amount of exchange coupling in ruler **2**.

With our current set of RIDME background data it is difficult to predict the minimal delay t_1 after which the RIDME background shape is well represented by a stretched exponential. For an appropriate setup we recommend to measure a 3-pulse refocused Hahn echo decay (pulse sequence: $\pi/2 - \tau - \pi - 2\tau - \pi - \tau -$det) prior to setting up a RIDME experiment. We observed that the minimal t_1 required for reliable RIDME experiments is given by the time τ after which the ESEEM oscillations in the 3-pulse refocused Hahn echo decay are not visible anymore. Another option is to measure RIDME background decays with different t_1 values for the isolated particular paramagnetic species used for RIDME detection in the system of interest to find the appropriate choice of t_1.

Note that in the RIDME background measurements also a signal consistent with ^{14}N ESEEM was observed, but this contribution was rather weak compared to the overall deviation of the background fit from the stretched exponential shape. This ^{14}N ESEEM contribution also remained, when the bi-stretched exponential fit is performed (see SI1 Figure 17(A)). To exclude the nitrogen nucleus of the nitroxide as the source of the background artefact we performed RIDME background measurements on nitrogen-free trityl radicals. No ^{14}N ESEEM was observed, but the background artefact remains (SI1 Figure 17(B)). In the Fourier spectrum of the experimentally detected background decays no other specific frequencies corresponding to any relevant magnetic nuclei were observed.

All tested RIDME experiments in the frozen solutions of nitroxide radicals and also Finland trityl radicals (see SI1 Fig. 17 for the trityl RIDME data) contain the background artefact, and at the same time, the corresponding radicals have a relatively large set of intramolecular hypefine couplings. In the Finland trityl radical used here as a comparison to nitroxides, the magnetic nuclei are on average more remote from the electron spin and also more symmetrically distributed around the localisation spot of the unpaired electron. Furthermore, RIDME data for trityl were recorded at 80K due to the radical's very slow longitudinal relaxation. At 80 K one can expect some averaging of the methyl proton couplings due to their partially unfrozen motion. In line with the hypothesis of the ESEEM origin of this artefact discussed in the manuscript, the background artefact is weaker in the Finland trityl sample as compared to nitroxide samples, where four methyl groups provide 12 protons, grouped in a define region in the close vicinity of the unpaired electron, and low experimental temperature ensured that these methyl groups make very limited motion. The arrangement of the methyl protons in nitroxide radical has also low symmetry with respect to the position of the unpaired electron, which should enhance the described effect.

Echo-crossing analysis

We computed the relevant echo-crossing points in 5-pulse RIDME according to the method reported in Gemperle *et al.* [32]. The nomenclature for the naming of echos in this work is given in SI-Table 2, and is based on the number of acting pulses, as well as the characteristic coherence order sequence.

The full list of 27 coherence order pathways which result in detectable coherence (-1), and which are in coherence order 0 during the mixing time, identified in this manner is given in SI-Table 3. The names of the pathways reflect the histories of the final detectable coherence, *e.g.* a Stimulated Echo ('SE') and a Stimulated echo of Hahn Echo ('SEHE') both refocus due to a stimulated echo ($pi/2 - \tau - \pi/2 - T - \pi/2 - \tau$-echo) refocusing condition, but the SEHE is generated from a coherence that has already been refocused as a Hahn echo once. The Refocused Stimulated Echo ('RSE'), in contrast, is a stimulated echo, that is then refocused by an additional π-pulse. In all our experiments we detected a Refocused Virtual Echo of Hahn Echo (RVEHE, in the literature - simply RVE[18]), which in the following we always denote as 'RIDME RVE' echo. Another echo, that would be modulated with the dipolar coupling as a function of the mixing block position is the Refocused Stimulated Echo of Hahn Echo (RSEHE, here RIDME*, in the literature RSE[18]), but it was not chosen for detection because this would not correspond to a constant-time experiment. [18]

For convenience, in this treatment we use the effective delays d_1 to d_5, which do not directly correspond to the experimental parameters ($t_1, t_2,...$), but can easily be converted, by making the identifications $d_1 = t_1$, $d_2 = t_1 + t$, and $d_2 = t_2 - t$. Note that $d_3 = T_{\text{mix}}$ is not relevant in our treatment. $\phi_{\text{d1}-\text{d4}}$ in Table 3 is the total phase accumulated in a pathway before d_5. An echo is observed for each pathway (except FID-type pathways) when $d_5 = \phi_{\text{d1}-\text{d4}}$, where d_5 is the acquisition delay after the last π pulse. To relate this table to echo-crossing with the RIDME RVE echo we also report $\Delta\phi(t)$, which is the effective change of $\phi_{\text{d1}-\text{d4}}$ as a function of the mixing block position t, which affects simultaneously $d_2(t)$ and $d_4(t)$.

Eight of the pathways continuously acquire phase in the same propagation direction (coherence order always -1), and therefore never refocus (FID-like pathways, termed 'anti-echos' in Gemperle *et al.* [32]), and are neglected in our further analysis. The effect of the 8-step phase cycle on the remaining 18 echos can be seen by considering the coherence order changes involved in each pathway.

For all remaining pathways we can calculate echo-crossing points for any choice of experimental delays (t_1, t_2) using the phases in SI1-Table 3. Typically, one records also a few point before the zero-time of the RIDME experiment, which in this treatment would be represented by $t < 0$. Echo crossing with the RIDME RVE echo occurs when the refocusing condition is equal to that of the RIDME RVE echo, thus when $\phi_{d1-d4}^{\text{RIDME RVE}} = t2 = \phi_{d1-d4}^{\text{echo}}(t_1, t_2, t)$. The crossing time t_{cross} can be calculated by inserting the values from Table 3 and solving for t. For example taking the echo SE1 ($\phi_{d1-d4} = d_2 - d_4$) we find

$$t_2 = d_2 - d_4$$

$$= t_1 + t_{\text{cross}} - (t_2 - t_{\text{cross}})$$

$$= t_1 - t_2 + 2t_{\text{cross}}$$

we expect crossing with the RIDME RVE echo at

$$t_{\text{cross}}^{(\text{SE1})} = (2t_2 - t_1)/2,$$

after the RIDME zero-time ($t = 0$), independent of t_2.

We found three echos that cross in a time range, where they could be potential sources of the slowly oscillating background artefact: SE1 ($t_{\text{cross}} = (2t_2 - t_1)/2$), SE2 ($t_{\text{cross}} = (t_2 - t_1)$) and SE5 ($t_{\text{cross}} = t_1$); all three are of the stimulated echo type, and should in principle be cancelled by the 8-step phase cycle.

SE1 originates from the first π-pulse effectively acting as a $\pi/2$-pulse, then the mixing block working as regularly, and the last π pulse not acting at all (sub-sequence 'π'-d_2-π-d_3-π-d_4-d_5).

SE2 has the same origin as SE1 (first π-pulse nominally acting as a $\pi/2$-pulse), but the refocusing is achieved by the second π pulse wrongly acting as a $\pi/2$-pulse as well. This pathway should be rather unlikely.

SE5 is an interesting case, because it represents the fraction of spins for which all $\pi/2$-pulses act as expected, but for which both refocusing π-pulse are inactive. This corresponds to an effective 3-pulse RIDME sequence (which would have a dead-time problem with respect to the dipolar modulation zero-time). This pathway is expected to be relatively weak, because of the faster transverse relaxation in the absence of the two refocusing π-pulses, and because of the small fraction of spins which are unaffected by these two pulses.

The RIDME experiment under several experimental condition was recorded in 'transient' mode to detect individual echos. In the plotted experimental echo transients measured at 40 K (SI-Figure 22) we only observe SE1. The moderately strong intensity of SE1 could have been detected, because the probability of the π-pulse to act as an effective $\pi/2$-pulse may be rather high in the pulse side-bands which have reduced microwave power. No additional, unaccounted for echo was observed to which we could attribute the background artifact. In any case this would have to be an echo that crosses at a very shallow 'angle', if it were to affact such a large fraction of the RIDME trace, even if the crossing echo is broad. The crossing point for SE1 clearly is narrow, and there is no direct reason why this echo should induce also significant alteration of the RIDME trace other than at t_{cross}. We thus exclude a direct echo crossing artifact as a source of the low frequency background artefact.

We nonetheless find that our identification of echos coincides exactly with the experimentally observed echos (see SI1 Figure 22). The commonly used 8-step phase cycle,[18] as well as an extended 32-step phase cycle to remove the additional echo crossing at $t_1 = t_2$ in the Bruker PulsSPEL format are given below. Note that by convention the channels that are not written fully are extended automatically by duplication to reach appropriate length.

```
begin lists "8-step"          begin lists "32-step"
 ph1 +x +x +x +x -x -x -x -x   ph1 +x +x +x +x -x -x -x -x
 ph2 +x -x +y -y +x -x +y -y   ph2 +x -x +y -y +x -x +y -y
 ph3 +x +x +x +x +x +x +x +x   ph3 +x +x +x +x +x +x +x +x -x -x -x -x -x -x -x -x +y +y +y +y +y +y +y +y -y -y -y -y -y -y -y -y
 asg1 +a +a +a +a -a -a -a -a  asg1 +a +a +a +a -a -a -a -a +a +a +a +a -a -a -a -a -a -a -a -a +a +a +a +a -a -a -a -a +a +a +a +a
 bsg1 +b +b +b +b -b -b -b -b  bsg1 +b +b +b +b -b -b -b -b +b +b +b +b -b -b -b -b -b -b -b -b +b +b +b +b -b -b -b -b +b +b +b +b
end lists                     end lists
```

Chirp Excitation

All experiments described in this section were performed at a home-built X/Q-band coherent AWG spectrometer described in Doll and Jeschke[23] and Doll and Jeschke[30]. The spectrometer is operated with home-written Matlab scripts, that were extended from existing scripts in the group. To set up the chirped RIDME RVE echo we first opimised the individual chirp pulses. The pulse lengths ($\pi/2$ and long π: 150 ns, short π: 75 ns), bandwidths (400 MHz for ruler **1**, resp. 450 MHz for ruler **2**), and rise-times (30 ns (long pulses), resp. 15 ns (short pulse)) were already fixed at this step. The chirp pulses were implemented as linear up-sweeps, with a quater-sine rise period to suppress ripples in the excitation profile, which are expected from the steep pulse flanks in the time-domain. Shorter rise times typically gave significantly less uniform excitation as seen by pulse profile experiments (explained below). The chirp pulses were performed with resonator compensation. The resonator profile[2] was obtained by the following procedure: first, we optimised

SI1 Tab. 2 Echo abbreviations definitions (only pathways that result in coherence order -1); the names aim to intuitively reflect the history of the final coherence order, and may not follow previously reported conventions. For example the 'Stimulated Free Induction Decay (SFID)' pathway behaves as a free induction decay pathway, but goes through a period coherence order 0. The effective pulse sequence that acts is also listed, as well as the coherence order path.

abbreviation	name	effective pulse sequence	coherence order path
FID	Free Induction Decay	$\pi/2$	-1
SFID	Stimulated Free Induction Decay	$\pi/2$- $\pi/2$-$\pi/2$	-1,0, -1
VFID	Virtual Free Induction Decay	$\pi/2$-$\pi/2$-$\pi/2$	-1, 0, -1
HE	Hahn Echo	$\pi/2$-π	1, -1
SE	Stimulated Echo	$\pi/2$-$\pi/2$-$\pi/2$	1, 0, -1
RSE	Refocused Stimulated Echo	$\pi/2$-$\pi/2$-$\pi/2$ - π	-1,0,1,-1
RVE	Refocused Virtual Echo	$\pi/2$-$\pi/2$-$\pi/2$ -π	1,0,1,-1
SEHE	Stimulated Echo of Hahn Echo	$\pi/2$-π-$\pi/2$-$\pi/2$	-1,1,0,-1
VEHE	Virtual Echo of Hahn Echo	$\pi/2$-π-$\pi/2$-$\pi/2$	1,-1,0,-1
RVEHE = RIDME RVE	Refocused Virtual Echo of Hahn Echo	$\pi/2$-π-$\pi/2$-$\pi/2$-π	-1,1,0,1 ,-1
RSEHE =RIDME*	Refocused Stimulated Echo of Hahn Echo	$\pi/2$-π-$\pi/2$-$\pi/2$-π	1,-1,0,1 ,-1

SI1 Tab. 3 Coherence order pathways for 5-pulse RIDME; for the generation of this table we assumed that we start from spins in thermal equilibrium (coherence order 0). We list only pathways that have coherence order 0 during the mixing block, and that result in coherence order -1 for detection. ϕ_{1-4} is the total phase accumulated in a pathway before d_5. $\Delta\phi(t)$ is the change of ϕ_{d1-d4} as a function of the mixing block position t, which affects simultaneously $d_2(t)$ and $d_4(t)$. Echo crossing with the RIDME RVE echo occurs when the total accumulated phase is equal to that of the RIDME RVE echo.

name	d1	d2	d3	d4	d5	ϕ_{d1-d4}	$\Delta\phi(t)$
SFID1	-1	-1	0	-1	-1	-d1-d2-d4	0
SFID2	-1	-1	0	0	-1	-d1-d2	-t
RSE1	-1	-1	0	1	-1	-d1-d2+d4	-2t
SFID3	-1	0	0	-1	-1	-d1-d4	t
SFID4	-1	0	0	0	-1	-d1	0
RSE2	-1	0	0	1	-1	-d1+d4	-t
SEHE1	-1	1	0	-1	-1	-d1+d2-d4	2t
SEHE2	-1	1	0	0	-1	-d1+d2	t
RVEHE = RIDME RVE	**-1**	**1**	**0**	**1**	**-1**	**-d1+d2+d4**	**0**
SFID5	0	-1	0	-1	-1	-d2-d4	0
SFID6	0	-1	0	0	-1	-d2	-t
RSE3	0	-1	0	1	-1	-d2+d4	-2t
FID	0	0	0	-1	-1	-d4	-t
FID	0	0	0	0	-1	-	0
HE	0	0	0	1	-1	d4	-t
SE1	0	1	0	-1	-1	d2-d4	2t
SE2	0	1	0	0	-1	d2	t
RVE1	0	1	0	1	-1	d2+d4	0
VEHE1	1	-1	0	-1	-1	d1-d2-d4	0
VEHE2	1	-1	0	0	-1	d1-d2	-t
RSEHE=RIDME*	1	-1	0	1	-1	d1-d2+d4	-2t
SE3	1	0	0	-1	-1	d1-d4	t
SE4	1	0	0	0	-1	d1	0
RVE2	1	0	0	1	-1	d1+d4	-t
SE5	1	1	0	-1	-1	d1+d2-d4	2t
SE6	1	1	0	0	-1	d1+d2	t
RVE3	1	1	0	1	-1	d1+d2+d4	0

the amplitude of a conventional spin echo (32/64 ns rectangular pulse lengths for $\pi/2$, resp. π pulse) microwave frequency that is approximately at the centre of the resonator profile (roughly estimated from echo intensity). At this step we also optimised the short repetition rate (24 ms was used at 20 K). With the rectangular pulses we then acquired a series of nutation experiments (β-1000 ns$\pi/2$-400 ns π, delays fixed), where the first pulse with uncalibrated flip angle *beta* was as hard as possible (5 ns pulse length, maximum amplitude). For each trace the microwave frequency and the magnetic field were stepped synchronously, to always excite nitroxide spins at the same resonance condition (approximately at the maximum of the nitroxide spectrum). The nutation oscillations were Fourier transformed to obtain the nutation frequencies, and only resonator positions with a nutation frequency larger than 5 MHz were considered for the continued analysis (which removes numerical instabilities). The resonator was characterised in this way over the full available frequency range of the AWG, typically at a microwave frequency resolution of 5 MHz. The non-linearity of the TWT amplifier was accounted for by a second nutation experiment, in which the amplitude of the inversion pulse was stepped over the whole available range. The required scaling coefficients for different microwave frequencies was calculated as a 4th-order polynomial fit to the amplitude stepped nutation experiment.[23] Resonator compensation was achieved by modulating the dwell time in the frequency sweep during the chirp pulse (compare middle panel (FM) in SI1-Figure 29).[30]

The amplitudes of the $\pi/2$ and the short π resonator compensated chirp pulses were then optimised first in a 2-pulse (Hahn echo) experiment with offset compensation (ensured by the 2:1 pulse length ratio). At this step we already included resonator compensation. With the optimised amplitudes from the 2-pulse echo, we optimised the long π pulse in a 3-pulse refocused echo experiment (2:2:1 pulse lengths).

The resulting excitation profiles of the pulses were again estimated by a series of nutation experiments with soft rectangular pulses as reported in for example Doll and Jeschke[23]. The excitation frequency of a soft pulse ($t_p = 64$ ns for inversion) was stepped together with the field position. The results for [Cu(II)-TAHA]-nitroxide **1** are shown in SI1 Figure 23(C), and for correct refocusing of the RIDME RVE echo we observed that it is important that the two π-pulses of different length perform approximately equally well.

As is described in the Experimental Section we performed RIDME with an offset-compensated 2:2:2:2:1 pulse length sequence[33]. There are two time dimensions in this experiment. One time dimension corresponds to the transient time of the RIDME RVE echo, which is here detected without boxcar integration. The second time dimension corresponds to the shift of the position of the mixing block in the RIDME pulse sequence (this can be referred to as the PDS time dimension). The resulting echos are very narrow in time-domain (see SI1 Figure 23(A)). The Fourier transform of the transient refocused virtual echo signal yields the spectrum of the excited spins, which as expected closely resembles the EDEPR spectrum of nitroxide (SI1 Figure 23(B) for [Cu(II)-TAHA]-nitroxide ruler **1**). We found that for sufficiently good refocusing it is very important to work with a resonator mode that is as flat as possible over the range of the NO spectrum. This comes typically at the cost of microwave pulse power, due to the reduced quality factor, and of sensitivity, because also the detection efficiency is proportional to the inverse width of the resonator profile. However, it is favourable for resonator compensation of the chirp pulses, which is difficult to achieve with steep flanks in the resonator profile. After the first FT we obtain at 2D-RIDME dataset with contributions from the background still included (see SI1 Figure 24 and SI1 Figure 26, respectively, for [Cu(II)-TAHA]-nitroxide **1**, and [Cu(II)-PyMTA]-nitroxide **2**. The background is removed by division by a stretched exponential fit, which results in a 2D-RIDME form factor (SI1 Figure 25 and SI1 Figure 27, respectively for[Cu(II)-TAHA]-nitroxide **1**, and [Cu(II)-PyMTA]-nitroxide **2**). To obtain a 2D correlation plot, which is relating spectral position for the nitroxide detection to the corresponding dipolar frequency spectrum, the second Fourier Transform along the PDS time dimension is performed.
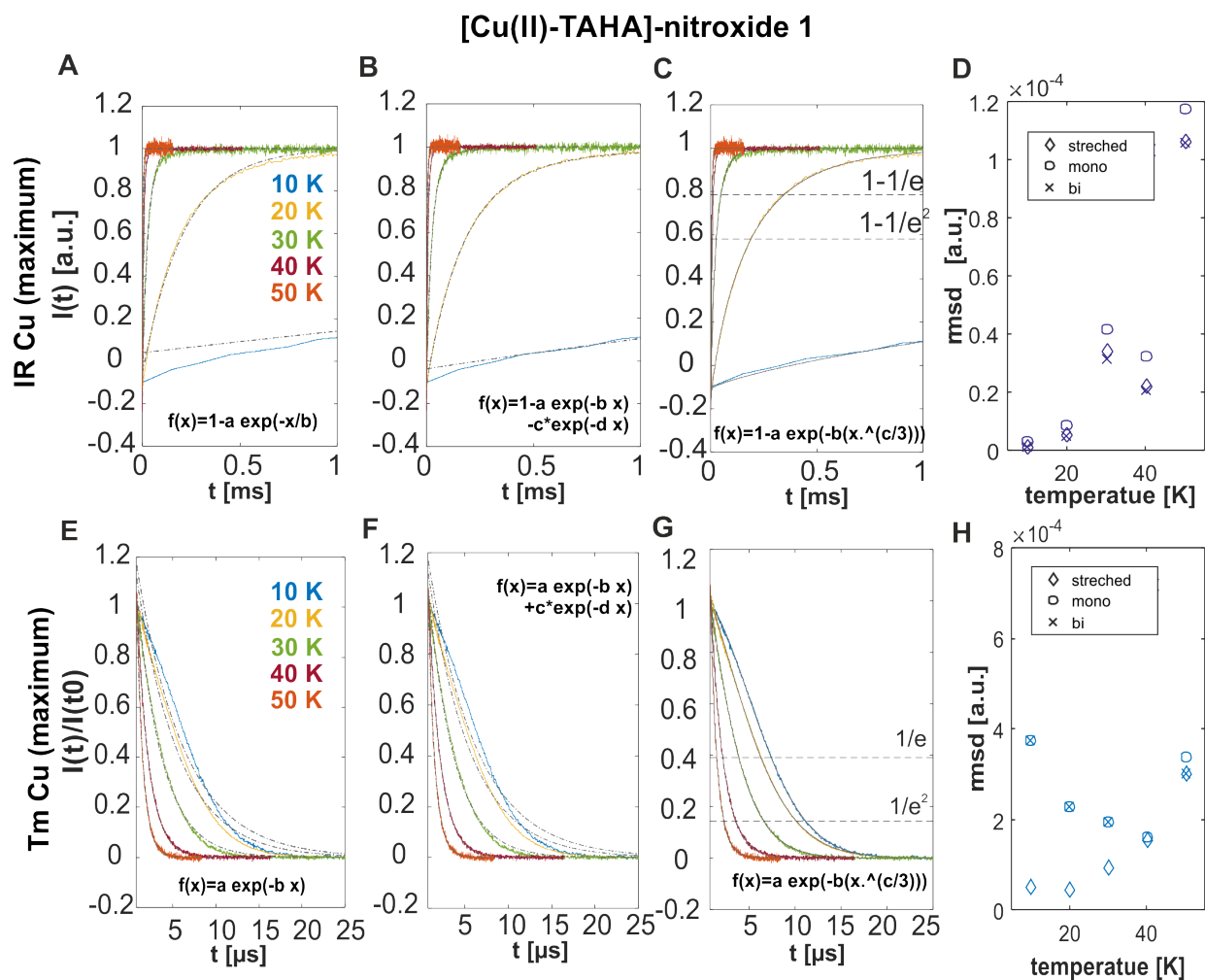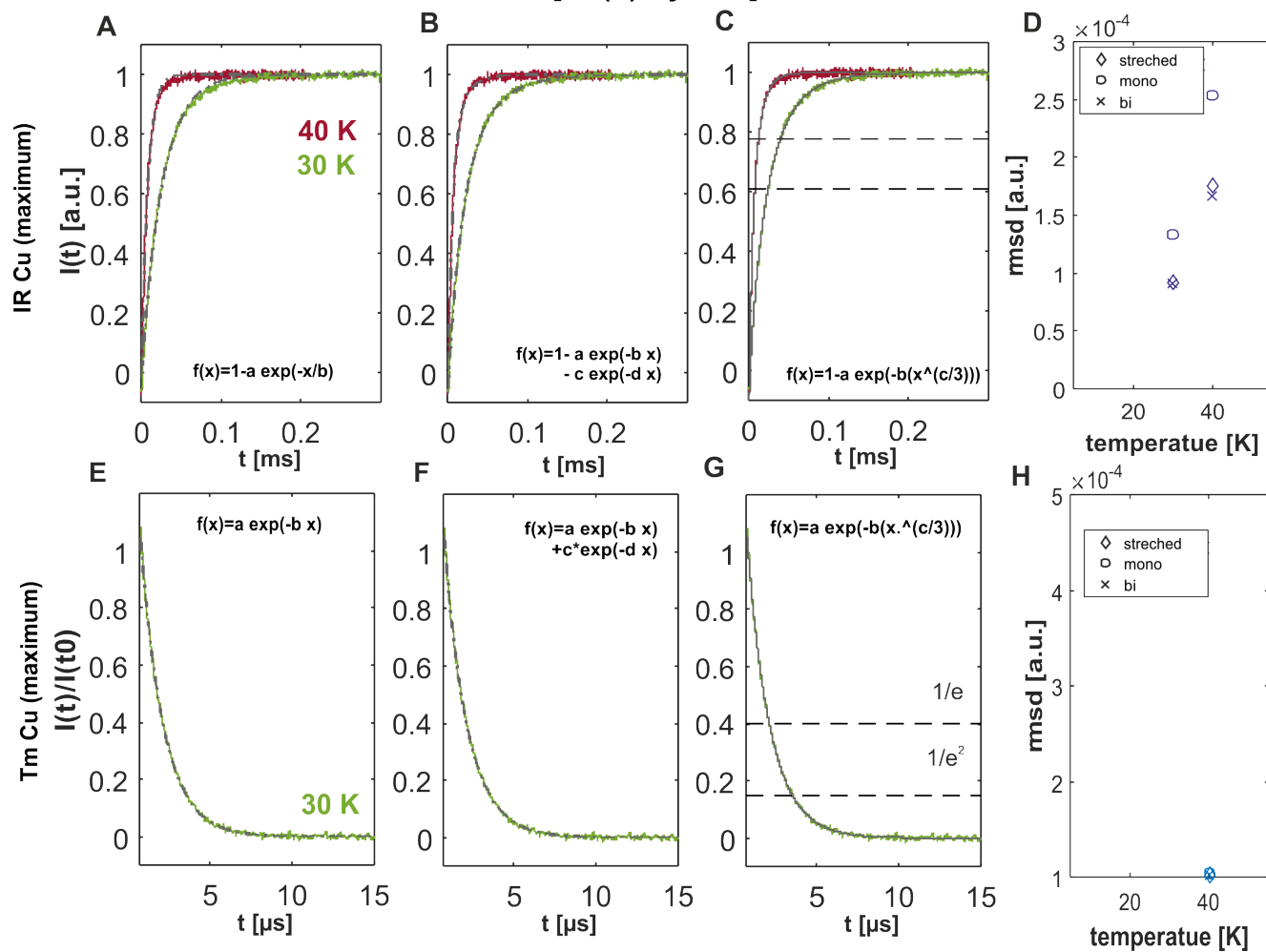
SI1 Fig. 3 Cu(II) IR (A-D) and T_m (E-G) measurements and fits for ruler **1** in the temperature range of 10 K-50 K. The dashed horizontal lines indicate the characteristic relaxation times reported in the main text. The fit model is given above each plot. The last plot in each row (D, resp. H) summarises the fit qualities. To this end we show the fit r.m.s.d. for the three fit models (linear vertical scale). The three models differ only slightly for the inversion recovery experiment at all temperatures. Strong differences, however, are observed for transverse relaxation, where a stretched exponential fit delivers significantly better results at temperatures below 40 K.
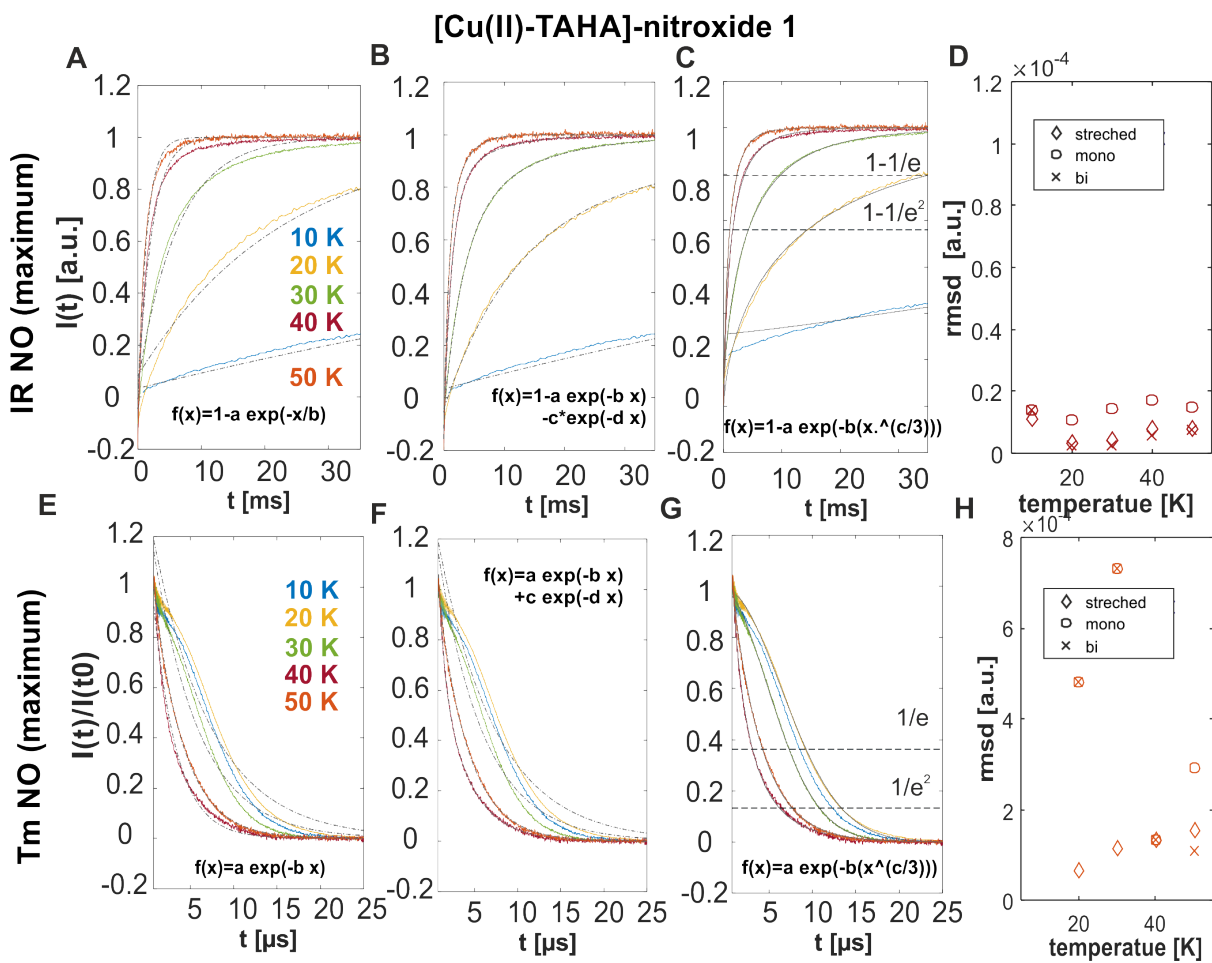
SI1 Fig. 4 Nitroxide IR (A-D) and T_m (E-G) measurements and fits for ruler **1** in the temperature range of 10 K-50 K. The dashed horizontal lines indicate the characteristic relaxation times reported in the main text. The fit model is given above each plot. The last plot in each row summarises the fit qualities. The last plot in each row (D, resp. H) summarises the fit qualities. To this end we show the fit r.m.s.d. for the three fit models (linear vertical scale). For nitroxide the bi-exponential model seems to be the best approximation at all temperatures. A stretched exponential is clearly best suited for fitting the transverse relaxation at temperatures below 40 K. At 40 K all models perform equally well.

[Cu(II)-PyMTA]-nitroxide 2

SI1 Fig. 5 Cu(II) IR (A-D) and T_m (E-G) measurements and fits for ruler **2**. The dashed horizontal lines indicate the characteristic relaxation times. The fit model is given in each panel. The last plot in each row (D, resp. H) summarises the fit qualities. To this end we show the fit r.m.s.d. for the three fit models (absolute values are not relevant).

[Cu(II)-PyMTA]-nitroxide 2
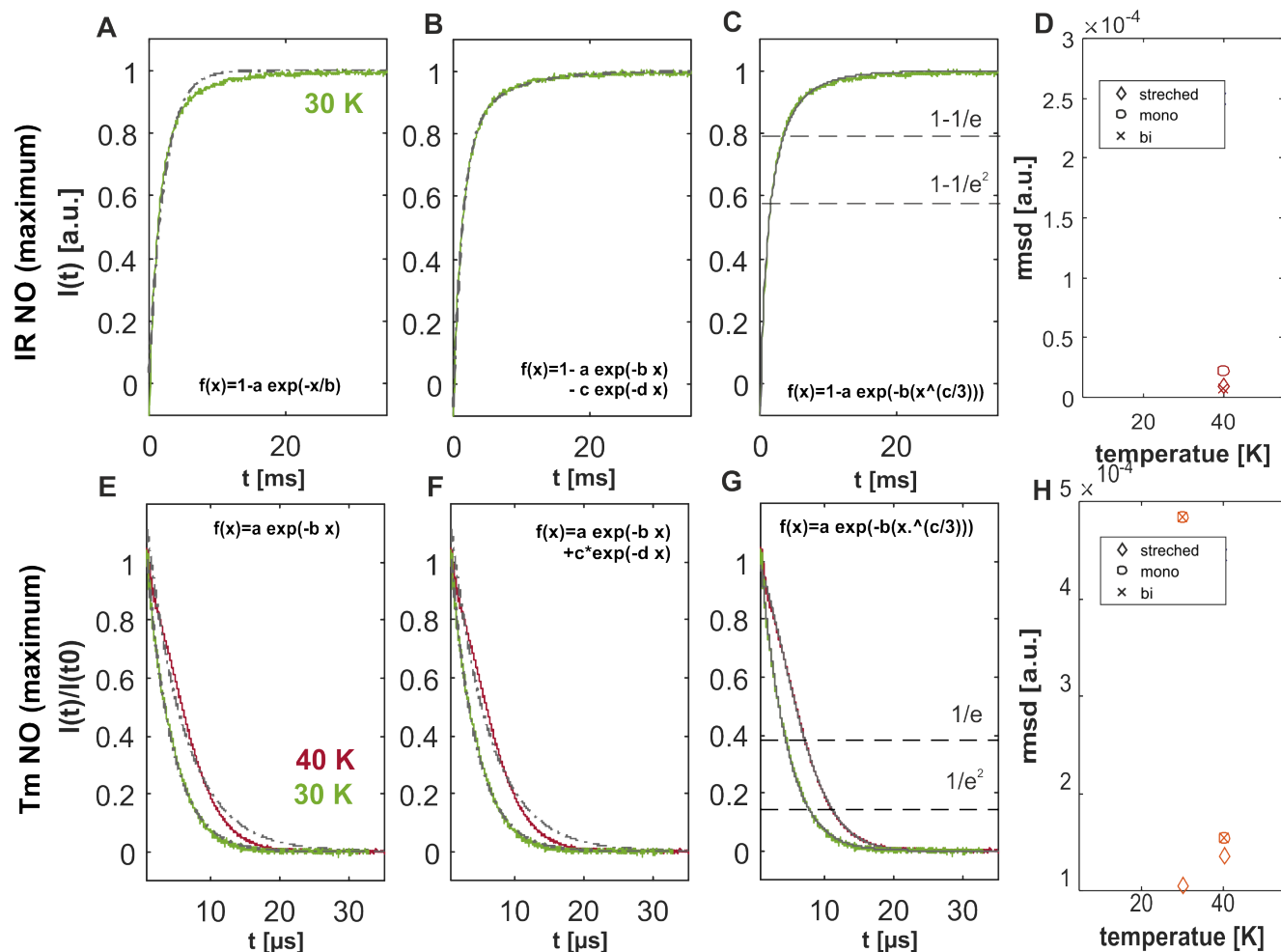
SI1 Fig. 6 Nitroxide IR (A-D) and T_m (E-G) measurements and fits for ruler **2**. The dashed horizontal lines indicate the characteristic relaxation times. The fit model is given in each panel. The last plot in each row (D, resp. H) summarises the fit qualities. To this end we show the fit r.m.s.d. for the three fit models (absolute values are not relevant).
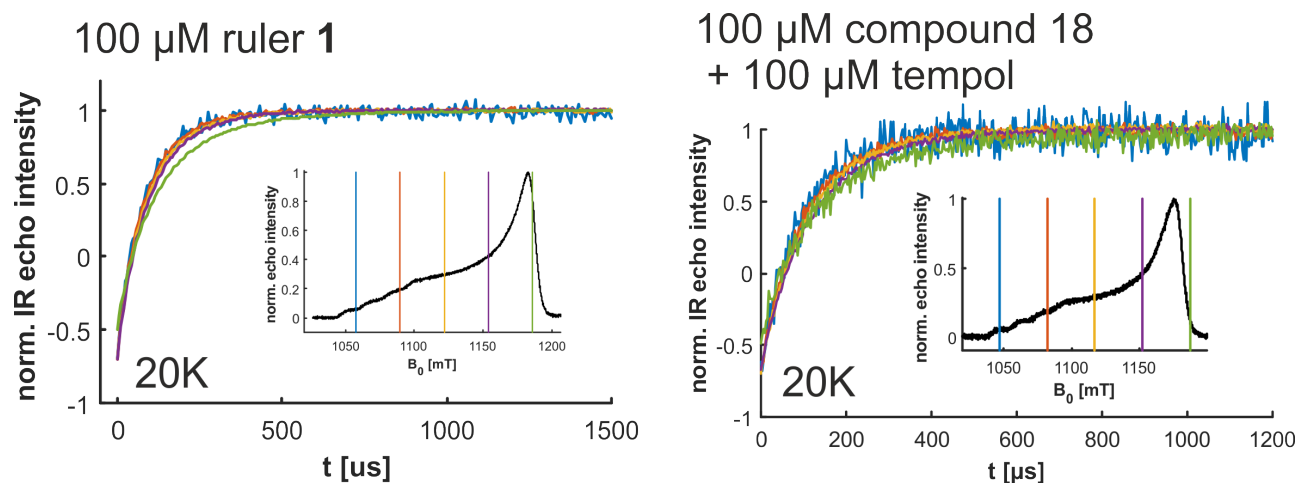
SI1 Fig. 7 Orientation dependent longitudinal relaxation of Cu(II) in ruler **1** (left), and in a reference sample (1:1 mixture of compound **18** and tempol) (right) at 20 K; Cu(II) oriented with the x/y-components of the hyperfine-, and g-tensor along B_0 (green curves) relaxes slightly more slowly than when oriented along the z-component (dark blue and orange).
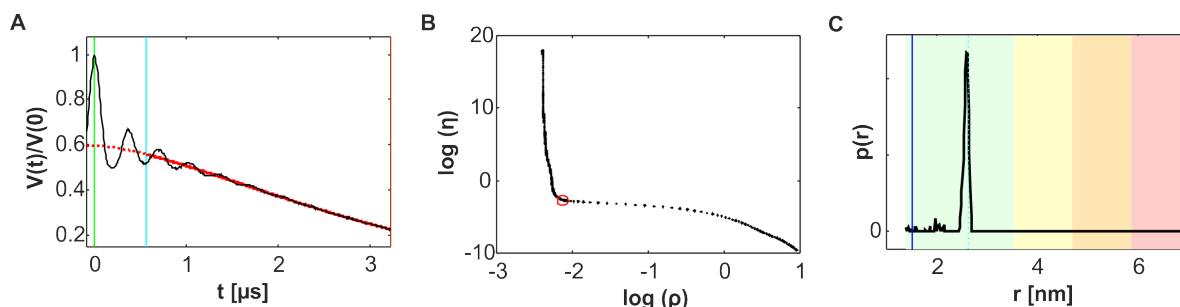
SI1 Fig. 8 Data processing in DeerAnalysis for RIDME (30 K, $t_1 = 4100\,\mathrm{ns}$, $t_2 = 3500\,\mathrm{ns}$) on ruler **1**. (A) Primary data (black) and fitting range (blue to orange line); stretched exponential fit (red). (B) The L-curve has a clear corner where the optimal regularisation parameter lies. (C) The distance distribution is fully in the safely detectable range.
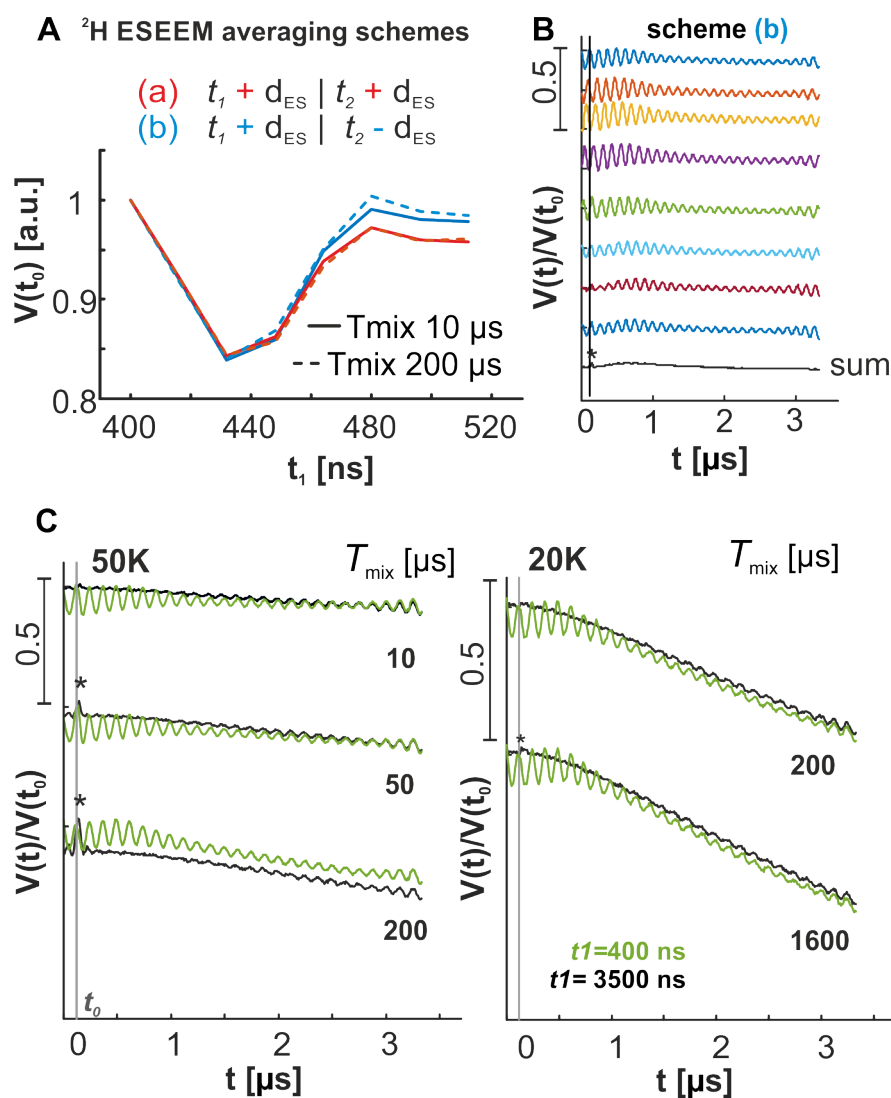
SI1 Fig. 9 Extended version of Figure 4 in the main text for ESEEM averaging. (A) and (C) are equivalent to what is shown in the main text figure. (B) shows the individual traces of the modified ESEEM averaging scheme. The summed trace is shown at the bottom and clearly contains a background artefact.

30K, Tmix 400µs 12/24 ns pulses

40K, Tmix 20 µs, 12/24 ns pulses
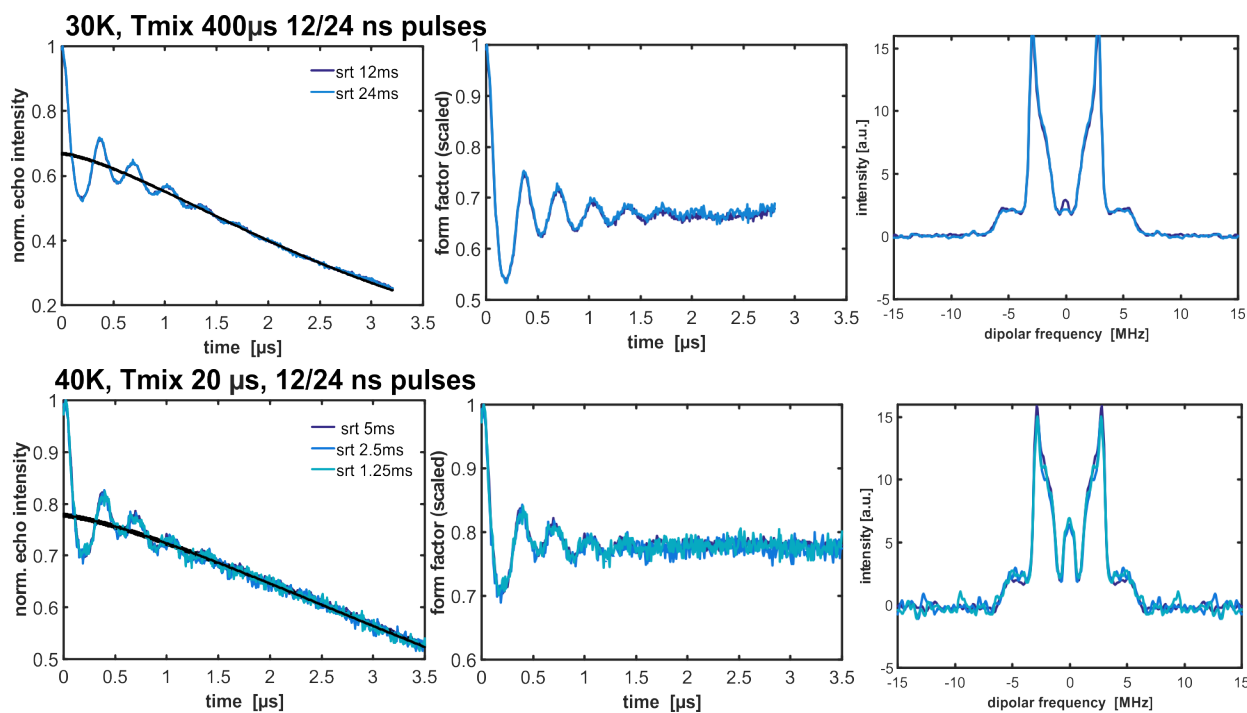
SI1 Fig. 10 The effect of measuring with saturation of the detected spins was evaluated at two conditions for ruler **1** (100 µM in deuterated solvent). Each trace was averaged for approximately the same amount of time. We clearly observe the expected decrease of SNR when using too short *srt*, but otherwise the signal is not altered within the precision of the noise. Note that the RIDME traces presented here were measured with short $t_1 = 400$ ns.
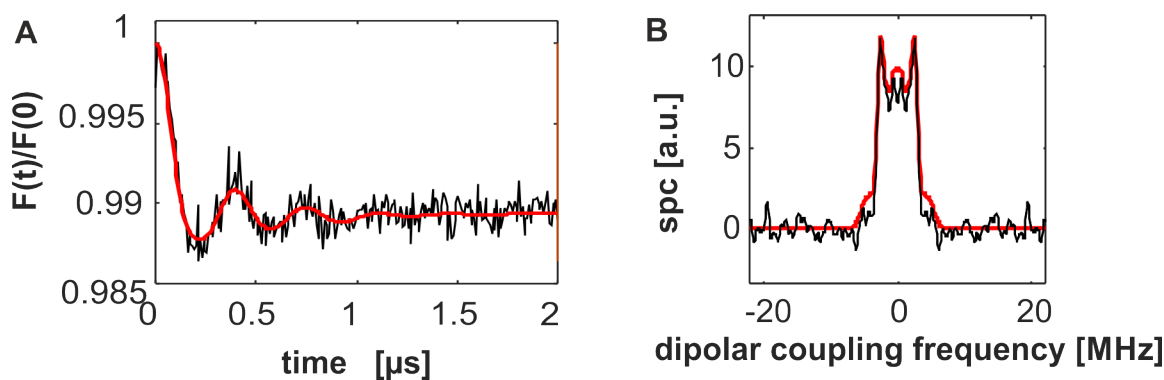
SI1 Fig. 11 (A) Form factor (black) and Tikhonov fit (red) of UWB-DEER on ruler **1** (B) corresponding dipolar spectrum
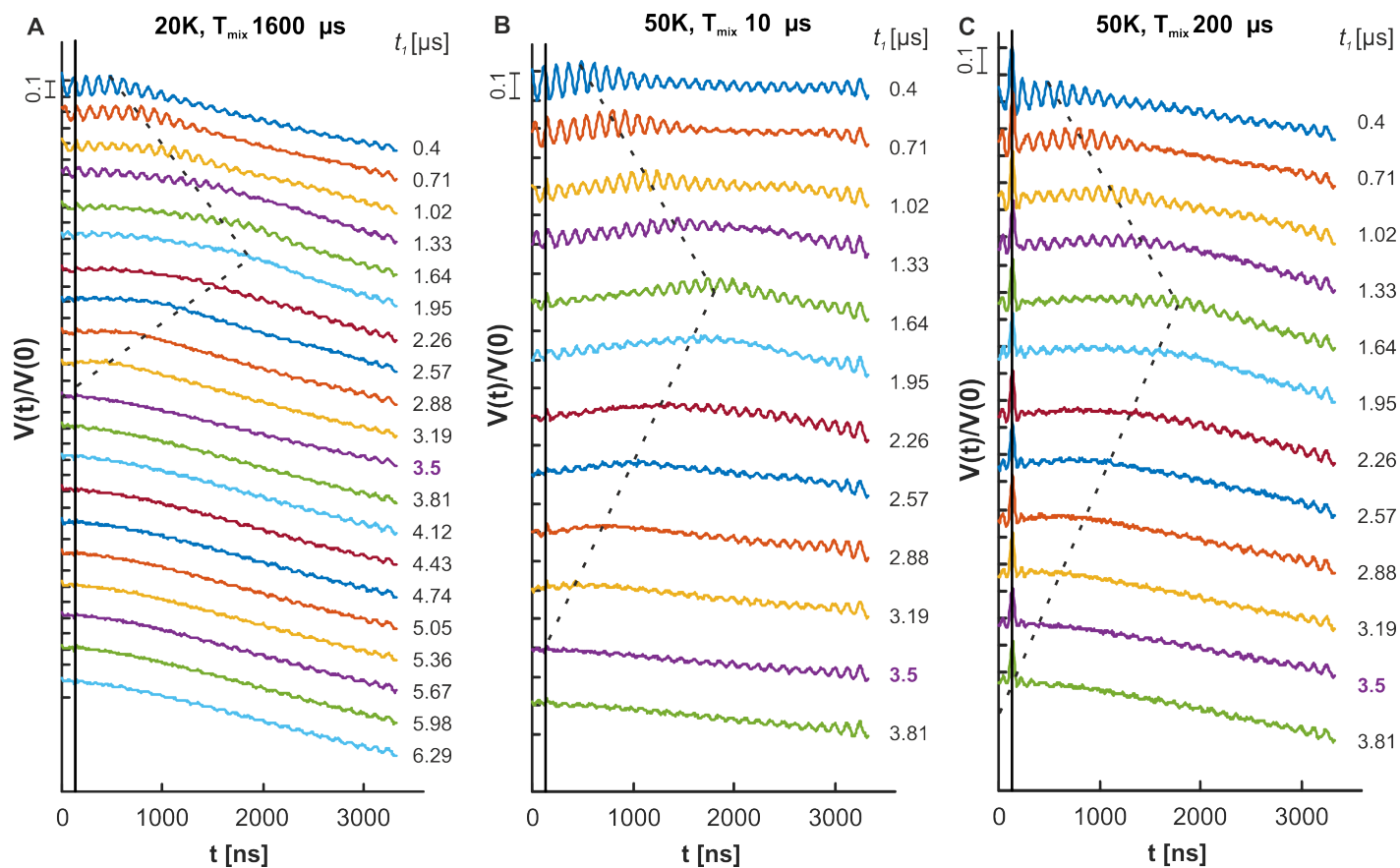
SI1 Fig. 12 RIDME background measurements on a mixture of tempol with [Cu(II)-TAHA] (**20**) in aqueous deuterated solvent at different temperatures and mixing times. The second refocusing delay in all traces was $t_2 = 3500$ ns. At 20 K (**A**) we used an initial t_1 of $t_1 = 400$ ns, which was incremented in steps of 310 ns to a final value of $t_1^{max} = 6290$ ns. For the measurements at 50 K (**B,C**) the same initial delay and increment was used, but we recorded traces only up to $t_1^{max} = 3810$ ns. The dashed lines are a guide to the eye for a 'ridge'-like feature in the shape of the background trace, which appears in all three tested conditions. The position of this component moves with t_1.
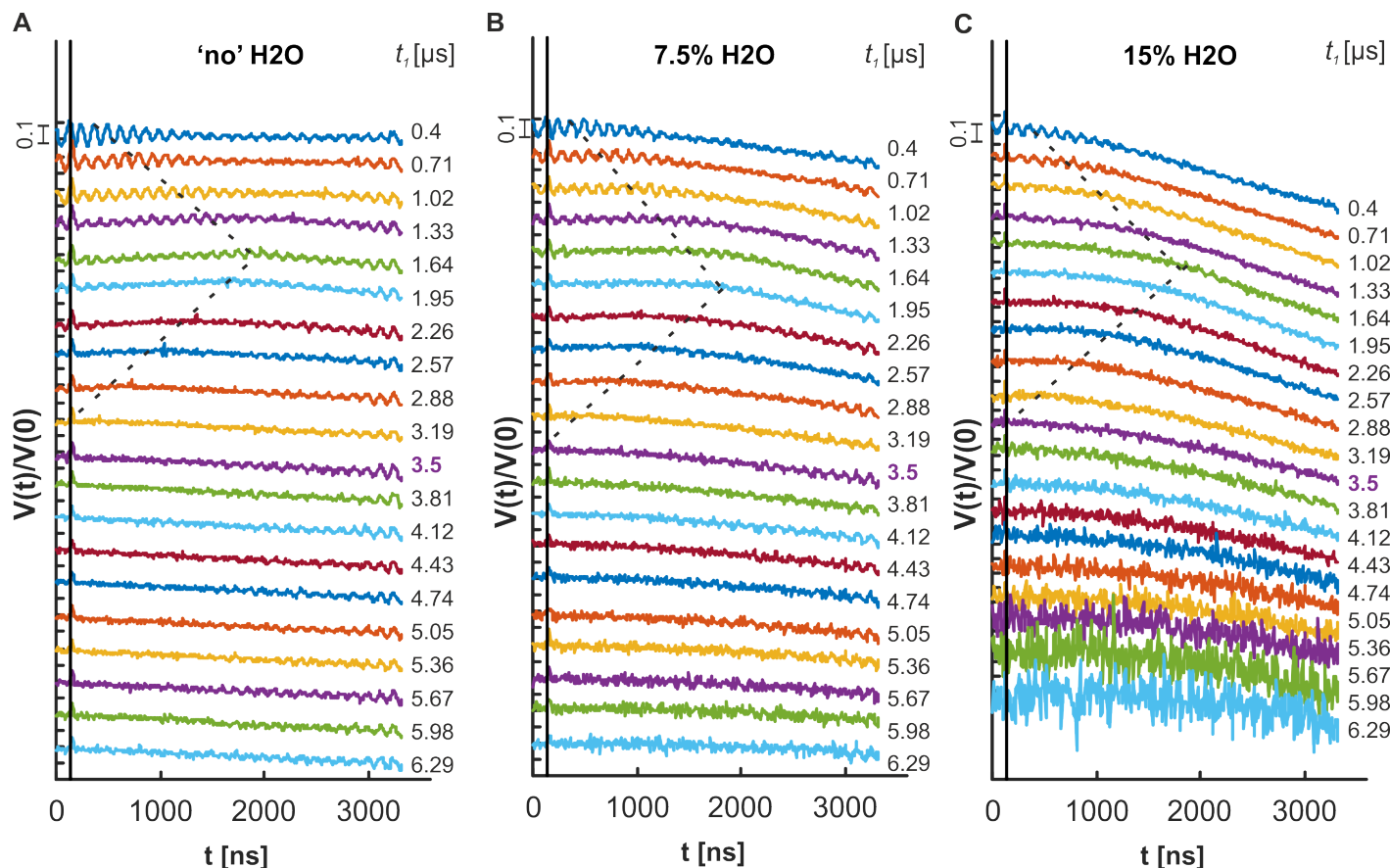
SI1 Fig. 13 RIDME background measurements on tempol in aqueous solvents of varying D_2O:H_2O ratios. The percentage given for each panel is the approximate volume concentration of H_2O in the total sample volume. In the traces from top to bottom the delay t is incremented from the starting value of $t_1 = 400\,\text{ns}$ in steps of $310\,\text{ns}$ to a final value of $t_1 = 6290\,\text{ns}$. t_2 is fixed at $3500\,\text{ns}$ in all traces. The dashed lines are a guide to the eye for a 'ridge'-like feature in the shape of the background trace. In the case of lowest degree of protonation (**A**) an additional dotted line indicates where a spike-like feature appears in the traces. SNR decreases in each series, since also $t_{\text{tot}} = t_1 + t_2$ increases. This is most strongly observed in the case of highest solvent protonation (**C**).
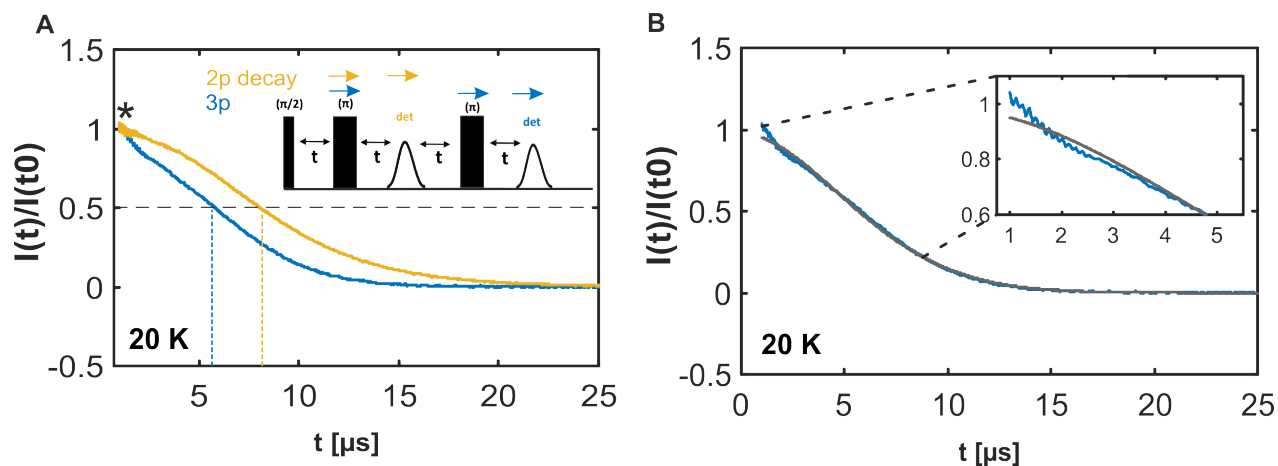
SI1 Fig. 14 Hahn echo decay (yellow) vs. 3p-echo decay (blue) measured for nitroxide on ruler **1** at 20 K. The signal has slightly lower intensity in the case of the 3p-echo decay. Furthermore, it is not a strictly monotonously decreasing function at early times, similar to the behaviour found in the RIDME background. A zoom-in on this region is shown in the right-hand-side graph. The monotonous decay is recovered after $\approx 4\,\mu\text{s}$ in this sample with fully deuterated solvent.
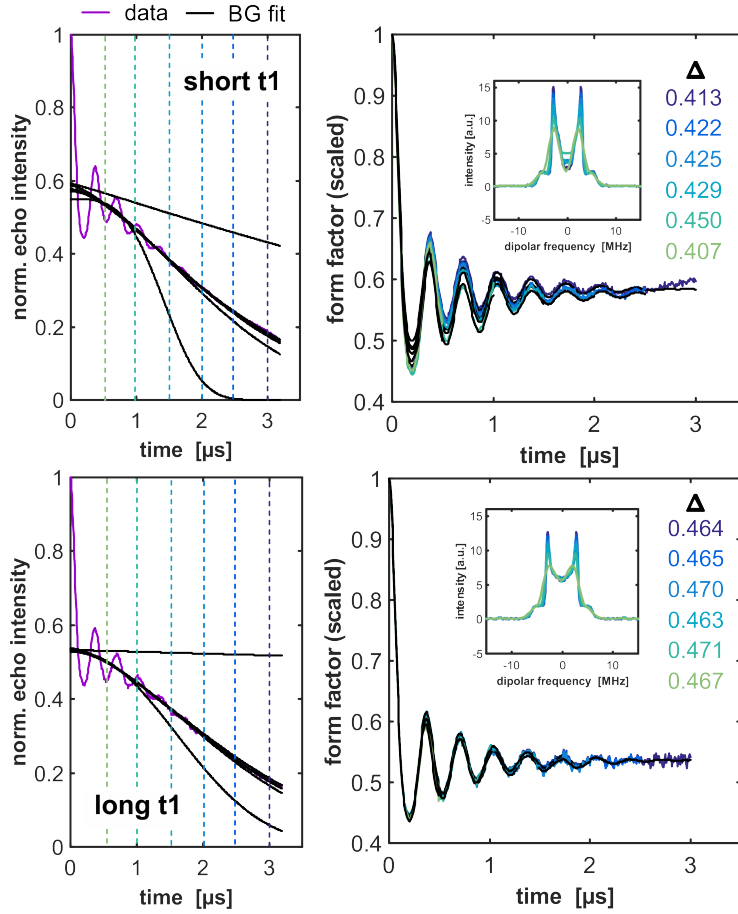
SI1 Fig. 15 RIDME experiments (20 K, $T_{mix} = 400\,\mu s$, experimental data in purple in top and bottom plot) measured on the same sample of ruler **1** in the same session with different choices of t_1 ('short': $t_1 = 400\,ns$, 'long': $t_1 = 4100\,ns$, $t_2 = 3500\,ns$ in both experiments). The vertical, coloured dashed lines indicate the range after which the data were truncated for BG fitting. The background fit with a stretched exponential (black lines) is highly sensitive to the exact fitting range with an unsuitable choice of t_1 (top), which leads to changes in the form factor and fluctuations in the modulation depth Δ.
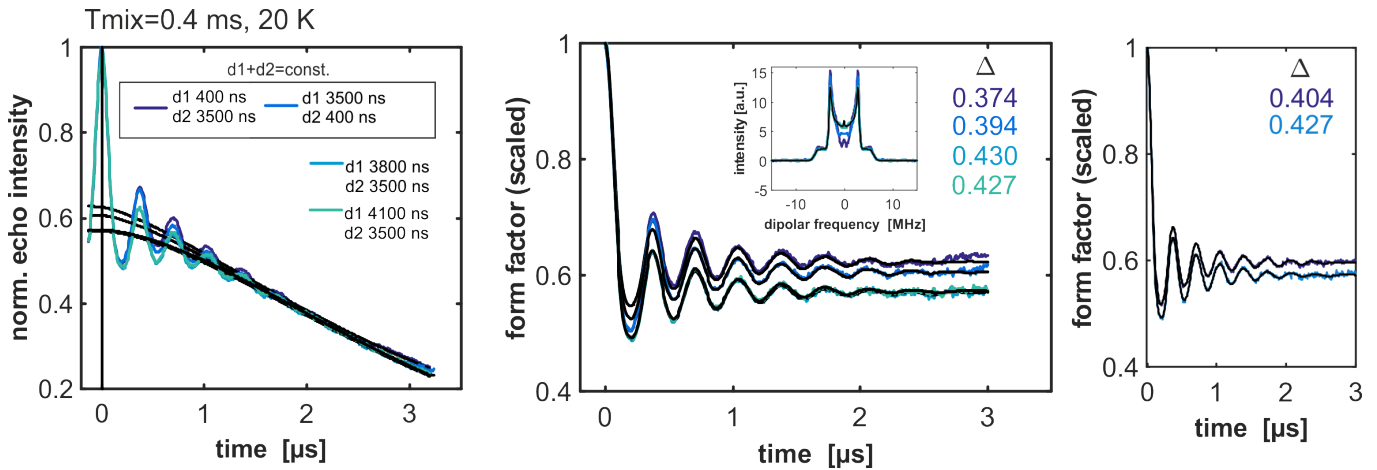
SI1 Fig. 16 Measuring with a long delay t_1 suppresses the slow-oscillation artefact in the background contribution even when the total transverse relaxation time is kept constant. Empirically we found that setting t_1 to fall into the range where the 3p echo decay is approximately linear (see SI-Figure 14) is required for acceptable suppression. At $t_1 = t_2$ the exact determination of the modulation depth may be compromised, due to an echo crossing with an unmodulated echo, which is not removed by the 8-step phase cycle.
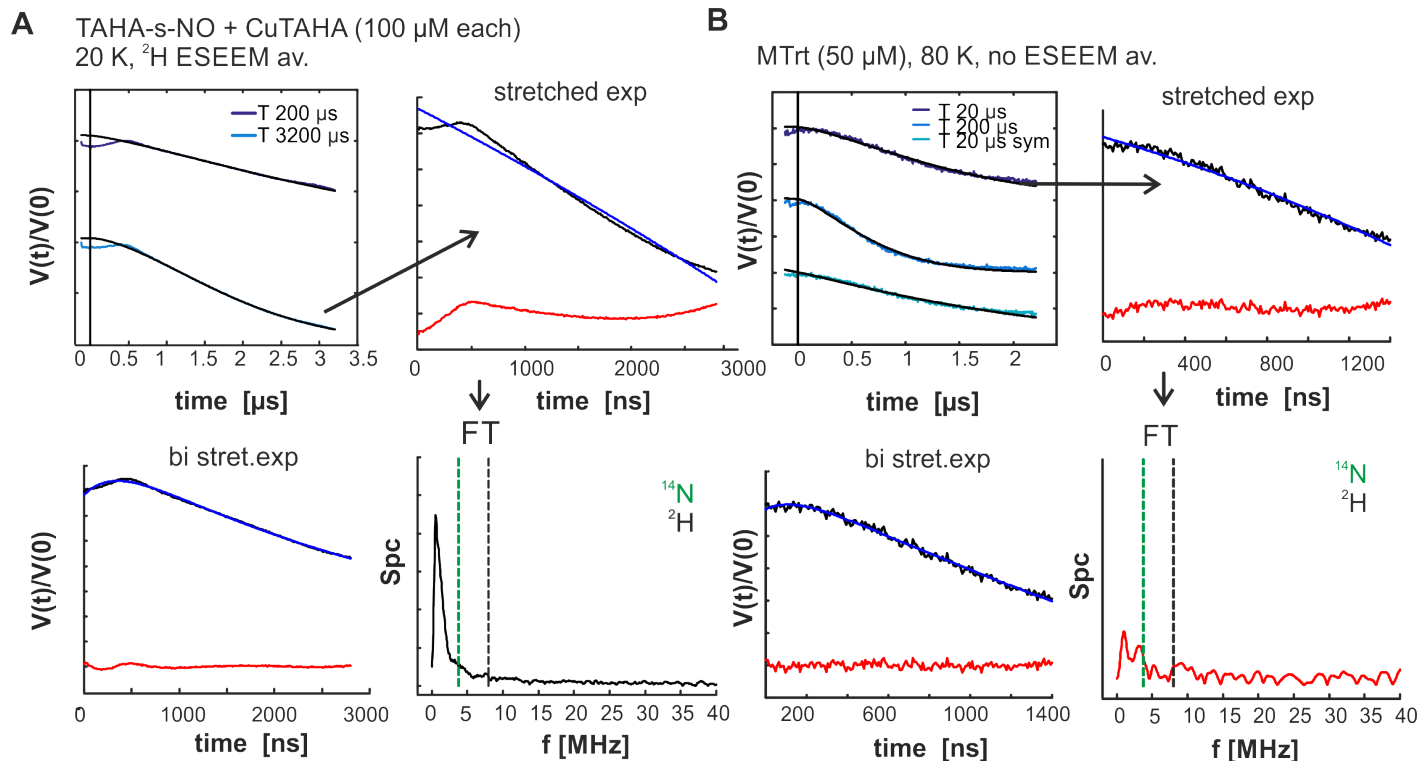
SI1 Fig. 17 (A) RIDME background measurements on a reference sample without visibly resolved dipolar oscillations. *top left*: primary data and stretched exponential BG fit as performed in DeerAnalysis (black); *top right*: primary data (black), stretched BG fit (blue) and BG corrected trace (red) for FT analysis; *bottom left*:primary data (black), bi-stretched exponential fit (blue) and BG corrected trace (red) the BG model fit is significantly improved, and a resolved frequency is observed in the residual; *bottom right* frequency spectrum after correction with stretched exponential, and application of a Hamming window (black), and lines to indicated expected ESEEM frequencies of common nuclei at Q-band (*e.g.*[1]H: 52.3 MHz, [2]H: 8.0 MHz, [14]N: 3.8 MHz, [15]N: 5.3 MHz, converted from tabulated nuclear frequencies using $B_0 = 1216.3$ mT). (B) (same composition of plots as in (A)): Spectral diffusion in the MTrt sample is much faster (i.e. steeper decays), and also cannot be fitted with a single stretched exponential (top right plot). The oscillation at the ^{14}N ESEEM frequency is not observed. (*e.g.e.g.*[1]H: 52.2 MHz, [2]H: 8.0 MHz, [14]N: 3.8 MHz, [15]N: 5.3 MHz, converted from tabulated nuclear frequencies using $B_0 = 1217.3$ mT).
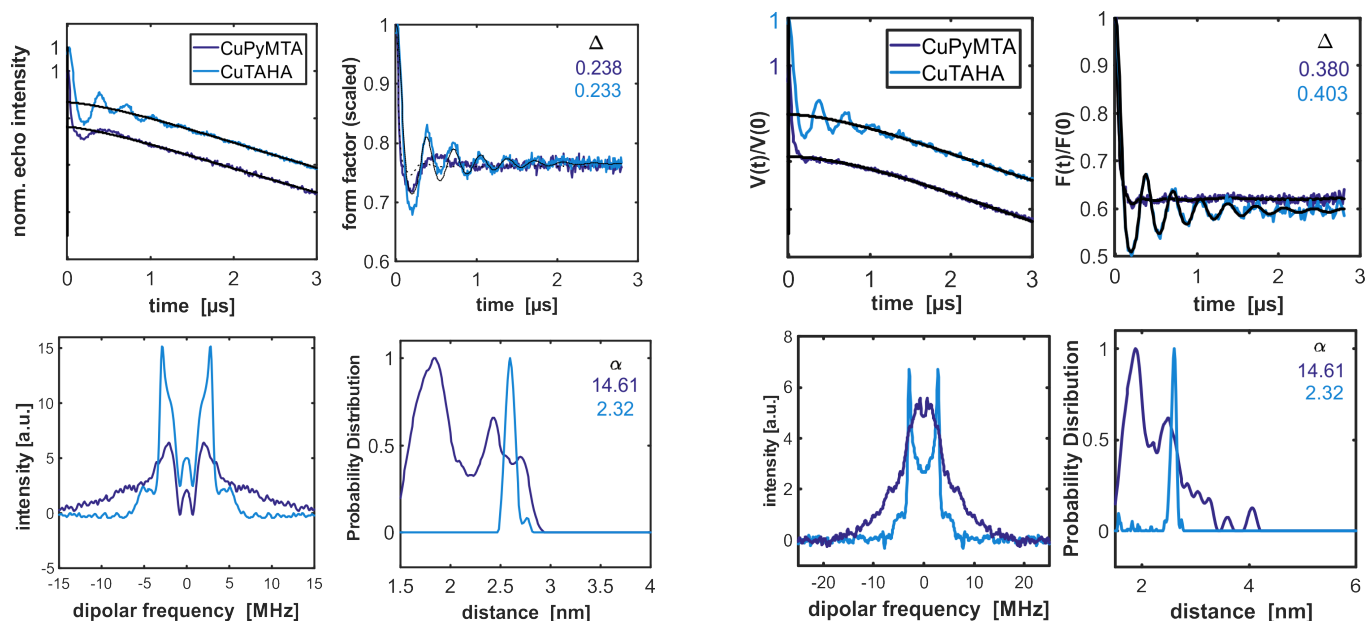
SI1 Fig. 18 Comparison of RIDME on rulers **1** and **2** that have the same spacer length but different Cu(II)-chelating ligands (blue: TAHA, purple: PyMTA) *left block*: measured at 40 K with short $t_1 = 400$ ns, *right block*: measured at 30 K with long $t_1 = 6100$ ns (same as figure in main text); in the case of PyMTA, the distance distribution fitted to the time-domain data is strongly biased by the presence of exchange coupling, and we observe a broad "ghost distance" peak with a maximum below 2 nm. In addition to a peak at approximately the expected true Cu(II)-nitroxide distance (2.5 nm), the background artefact leads to a third strong peak in the range above 2.5 nm. This is in fact still not fully suppressed in the measurement with long $t_1 = 6.1$ μs. This emphasises the importance of finding suitable measurement conditions when dealing with dipolar data without pronounced oscillations.
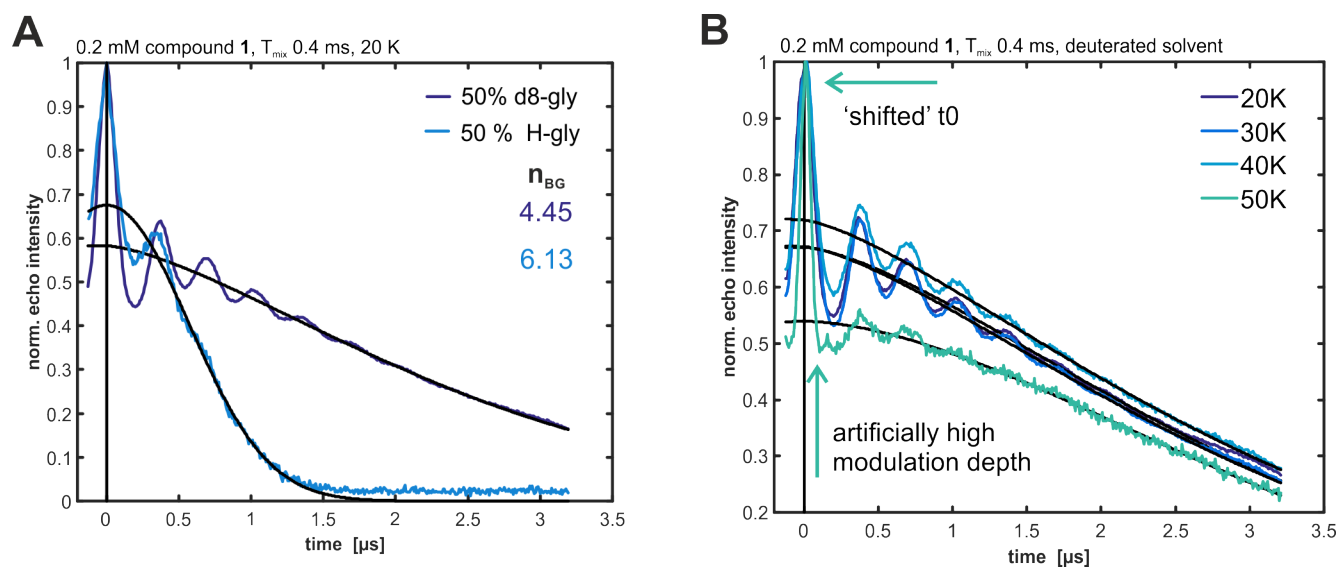

SI1 Fig. 19 RIDME on ruler **1** (A) The effect of solvent protonation is a much faster background decay. (B) At high temperatures an echo-crossing artefact causes a shift in the apparent zero-time, and an artificially high modulation depth.
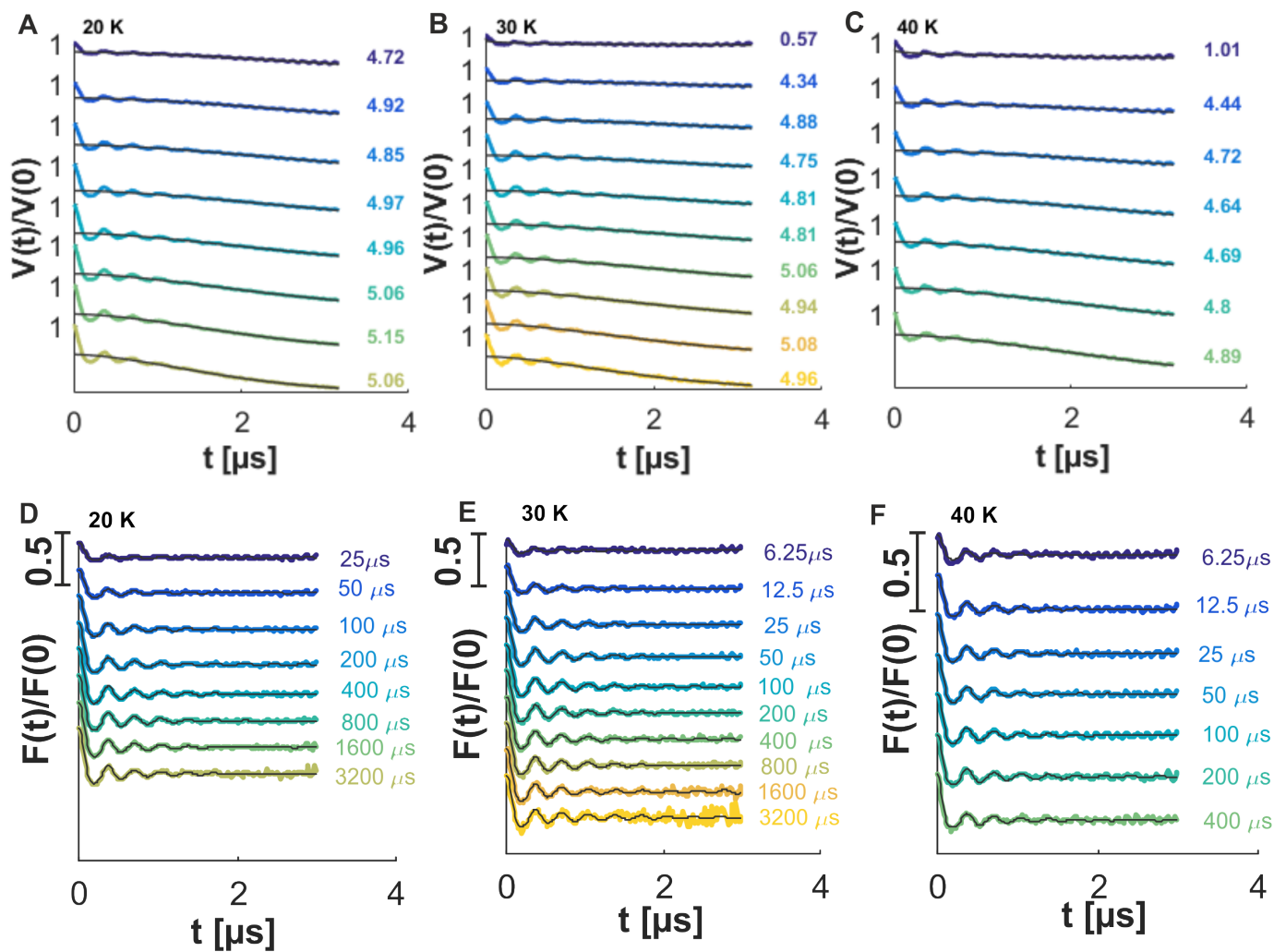
SI1 Fig. 20 RIDME with hard pulses ($t_1 = 4100\,\text{ns}$) on ruler **1** (A-C) Primary data at three temperatures and background fit. To the right of the data we give the fitted background dimensionality (D-E)Extracted form factors to (A-C). The mixing time is given to the right of the data.
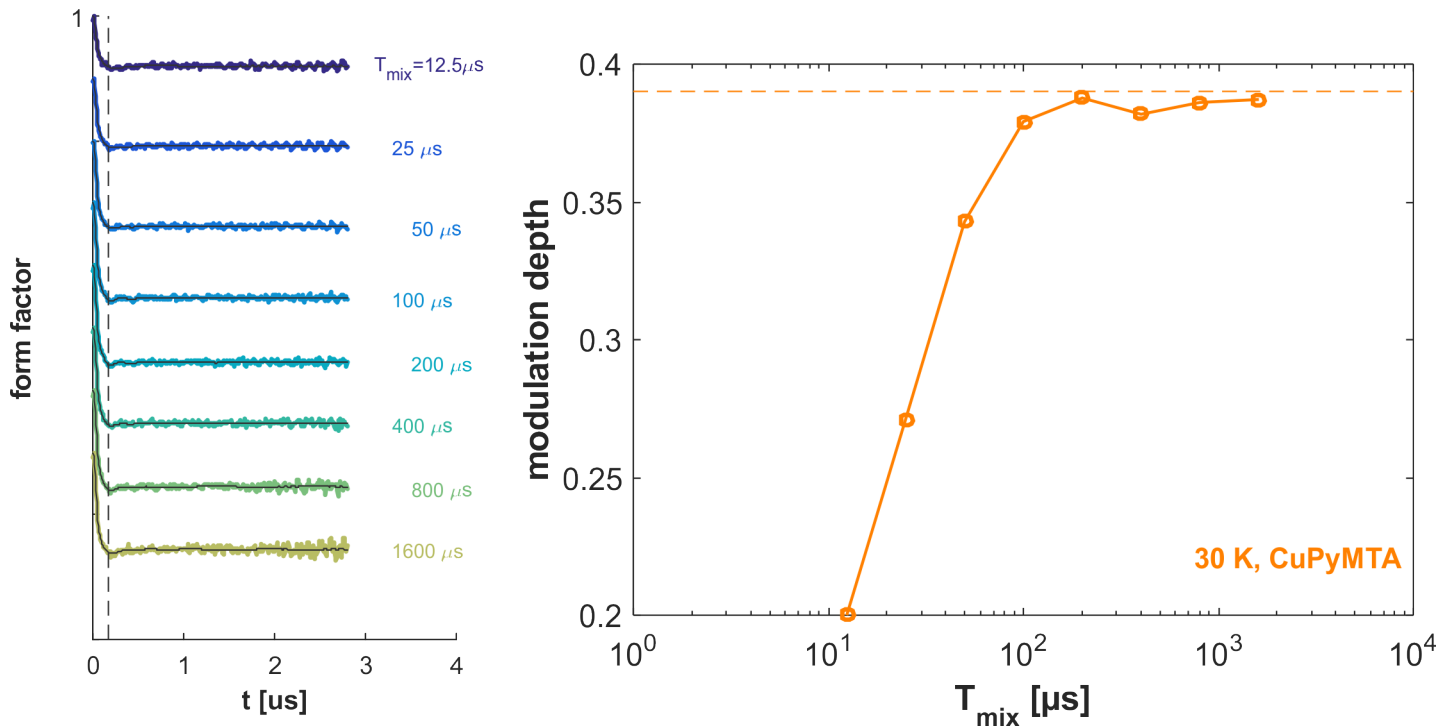
SI1 Fig. 21 RIDME ($t_1 = 6100\,\text{ns}$) on ruler **2** (carrying the PyMTA ligand) at 30 K as function of mixing time, and extracted modulation depth; same as with the TAHA ruler the modulation depth increases linearly with $\log(T_{\text{mix}})$, until it reaches a plateau. The plateau modulation depth ($\Delta_{\text{mix,plateau}} \approx 0.39$) is slightly lower than that for ruler **1** at equivalent experimental conditions.
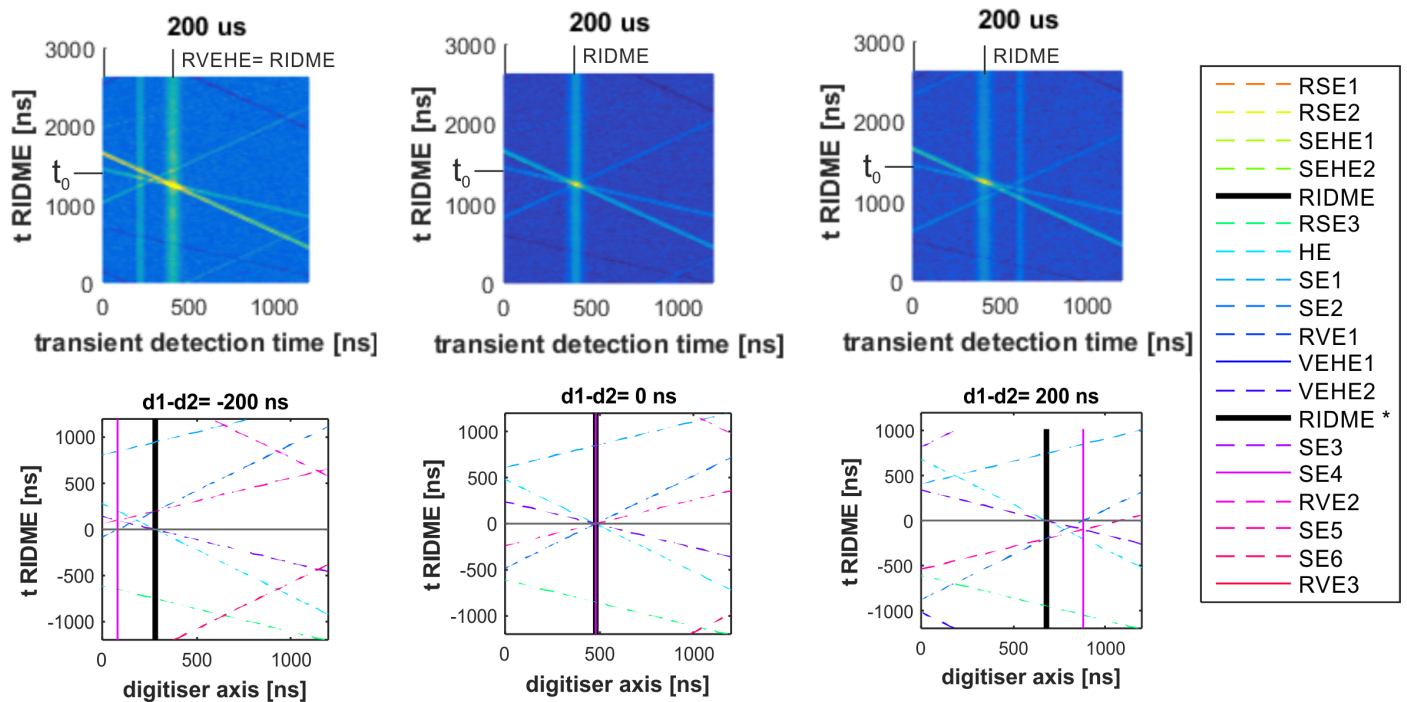

SI1 Fig. 22 *top*: Echo transients during a RIDME experiment (40 K) and *bottom*: simulated echo crossing pattern following the results in SI-Table 3. The dashed lines correspond to echos that should be removed by the 8-step phase cycle. From left to right the first refocusing delay $t_1 = \{1.5\,\mu\text{s}, 1.5\,\mu\text{s}, 1.5\,\mu\text{s}\}$ is increased while the second refocusing delay $t_2 = 1.5\,\mu\text{s}$ is kept constant. Note that in the experimental data the time is plotted as recorded, the zero-time is thus expected at t_1, while in the simulation we set the zero-time to $t = 0$. Furthermore, zero-time of the the digitiser axis for the simulated data does not follow the RIDME RVE echo, as it was done for the experimental data. At $t_1 = t_2$ RSE5 coincides with the RIDME RVE echo for all times t, and it is not removed by the 8-step phase cycle.
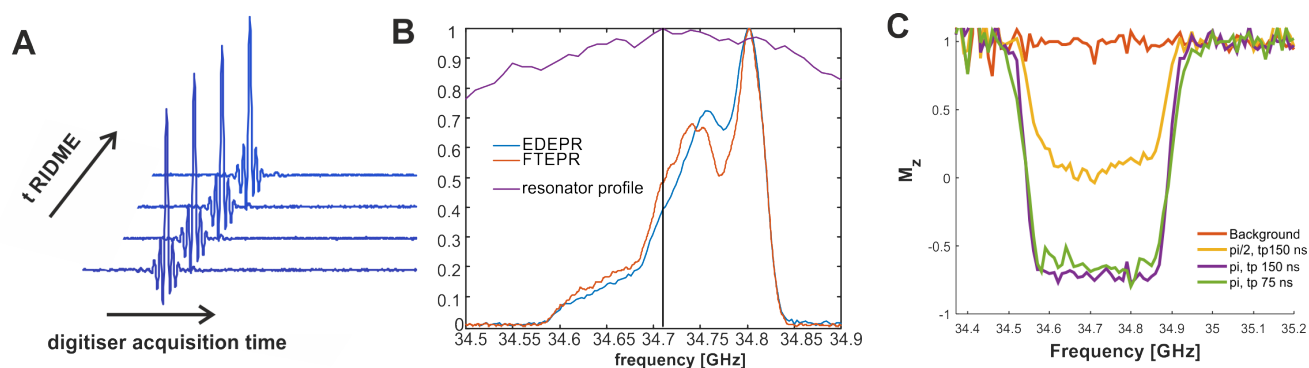
SI1 Fig. 23 (A) Digitally down-converted echo transients from the individual time-steps along the RIDME dimension can be Fourier transformed to yield the FT-EPR spectrum of the nitroxide of ruler **1**. (B) The Fourier transform (FT) of the echos yields the nitroxide spectrum (orange), which is in good agreement with the EDEPR nitroxide spectrum. The resonator profile is plotted on top in purple, and should to be set at flat as possible over the range of the nitroxide. The black vertical line indicates the centre of the resonator. (C) Resonator-compensated pulse profiles for the chirp pulses as determined from nutation experiments.[23] The long and short π-pulses perform similarly well, which is important for correct refocusing.
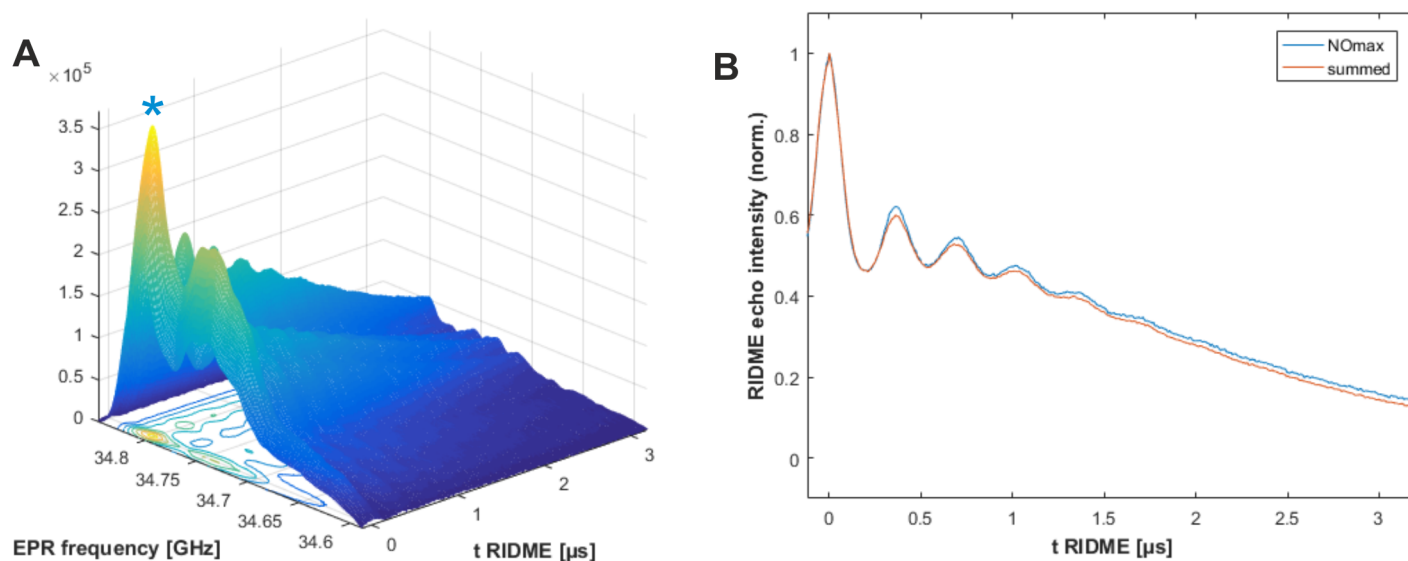

SI1 Fig. 24 [Cu(II)-TAHA]-nitroxide **1**; (A) Chirped RIDME traces after FT along EPR dimension; a RIDME trace is obtained for each resonance frequency within the nitroxide spectrum, which still contains the background contribution. (B) The background shape is similar over the whole range of the spectrum, which can be seen by comparing the summed trace (orange) to an individual slice at maximum of the nitroxide spectrum (blue, as indicated by star in (A))
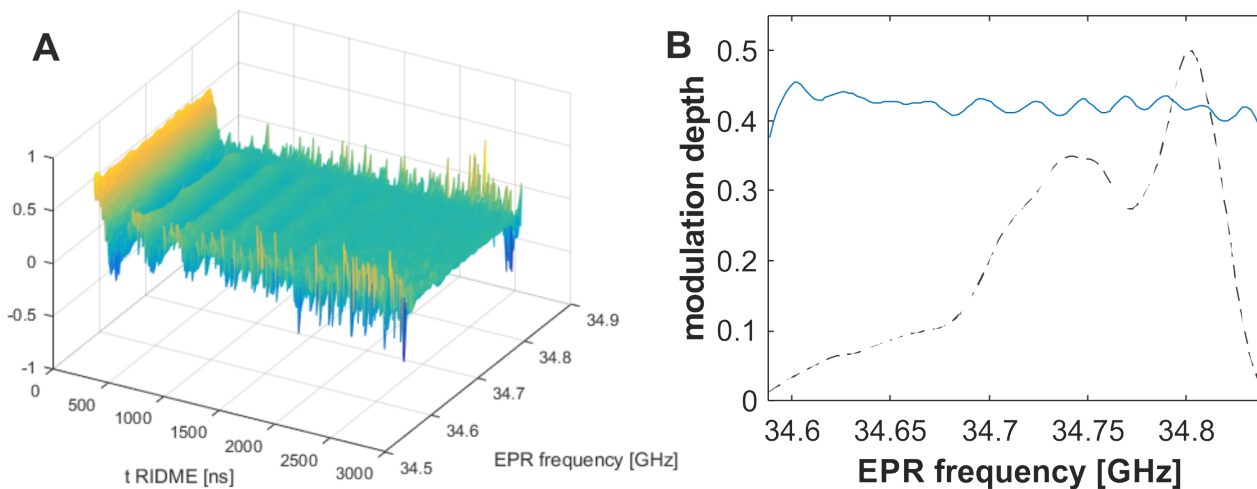
SI1 Fig. 25 [Cu(II)-TAHA]-nitroxide **1**; (A) Form factor after background correction. (B) The modulation depth is approximately constant over the range of the nitroxide spectrum. The oscillations in the modulation depth profile are due to variations in the background fit, and thus an artefact from the data processing.
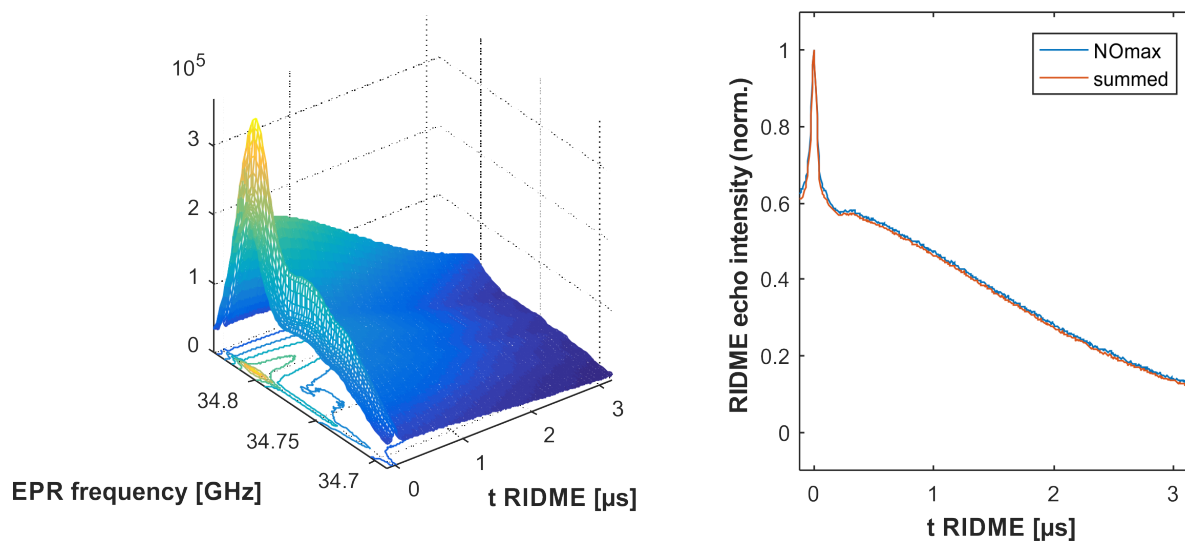

SI1 Fig. 26 [Cu(II)-PyMTA]-nitroxide **2**; (A) Chirped RIDME traces after FT along EPR dimension; a RIDME trace is obtained for each resonance frequency of nitroxide, which still contains the background contribution. (B) The background shape is similar over the whole range of the spectrum, which can be seen by comparing the summed trace (orange) to an individual slice at maximum of nitroxide (blue).
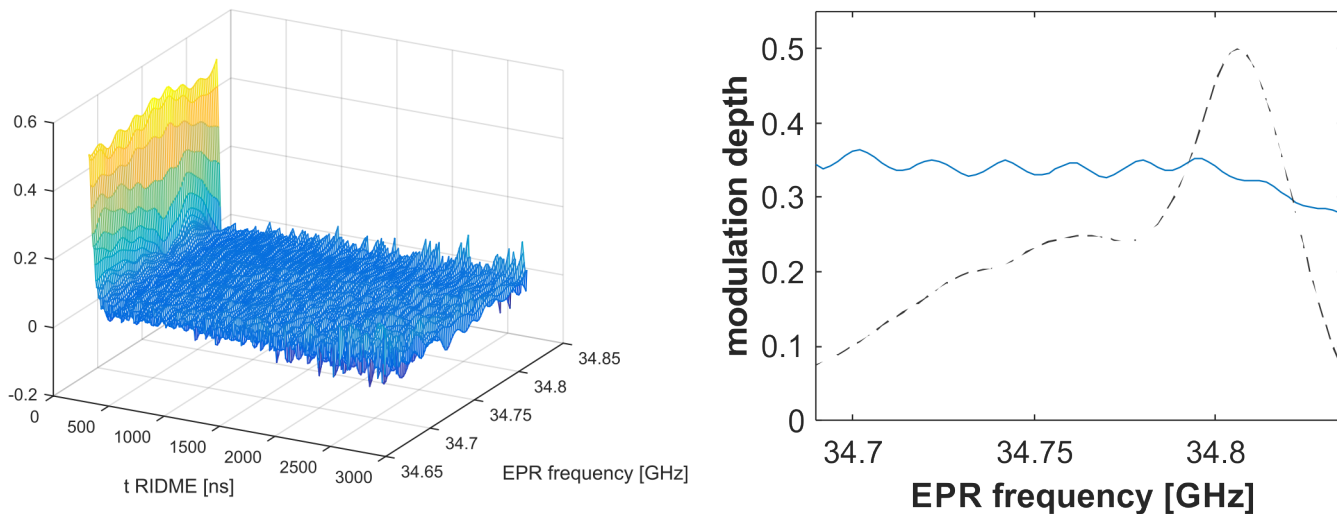
SI1 Fig. 27 [Cu(II)-PyMTA]-nitroxide **2**; (A) Form factor after background correction. (B) The modulation depth decreases slightly towards the high-frequency edge of the nitroxide spectrum. Similar as for ruler **1** we observe some aritfacts in the modulation depth profile originating from the background fitting.
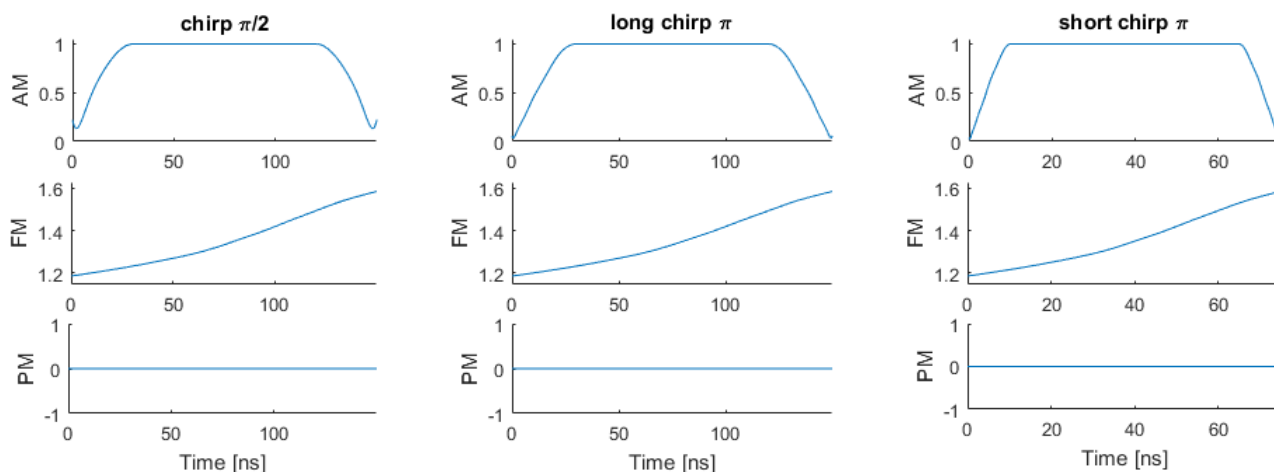
SI1 Fig. 28 Typical pulse shaping used for the chirp RIDME pulses *from left to right*: $\pi/2$ (150 ns, 30 ns rise time), long π (150 ns, 30 ns rise time), short π (75 ns, 15 ns rise time); *top to bottom*: amplitude modulation (AM), frequency modulation (FM) as synthesised by AWG (in GHz), phase modulation (PM); the quarter sine rise period of the amplitude profile attenuates ripples in the pulse profile. The frequency modulation serves to account for the resonator profile. No phase modulation was applied.
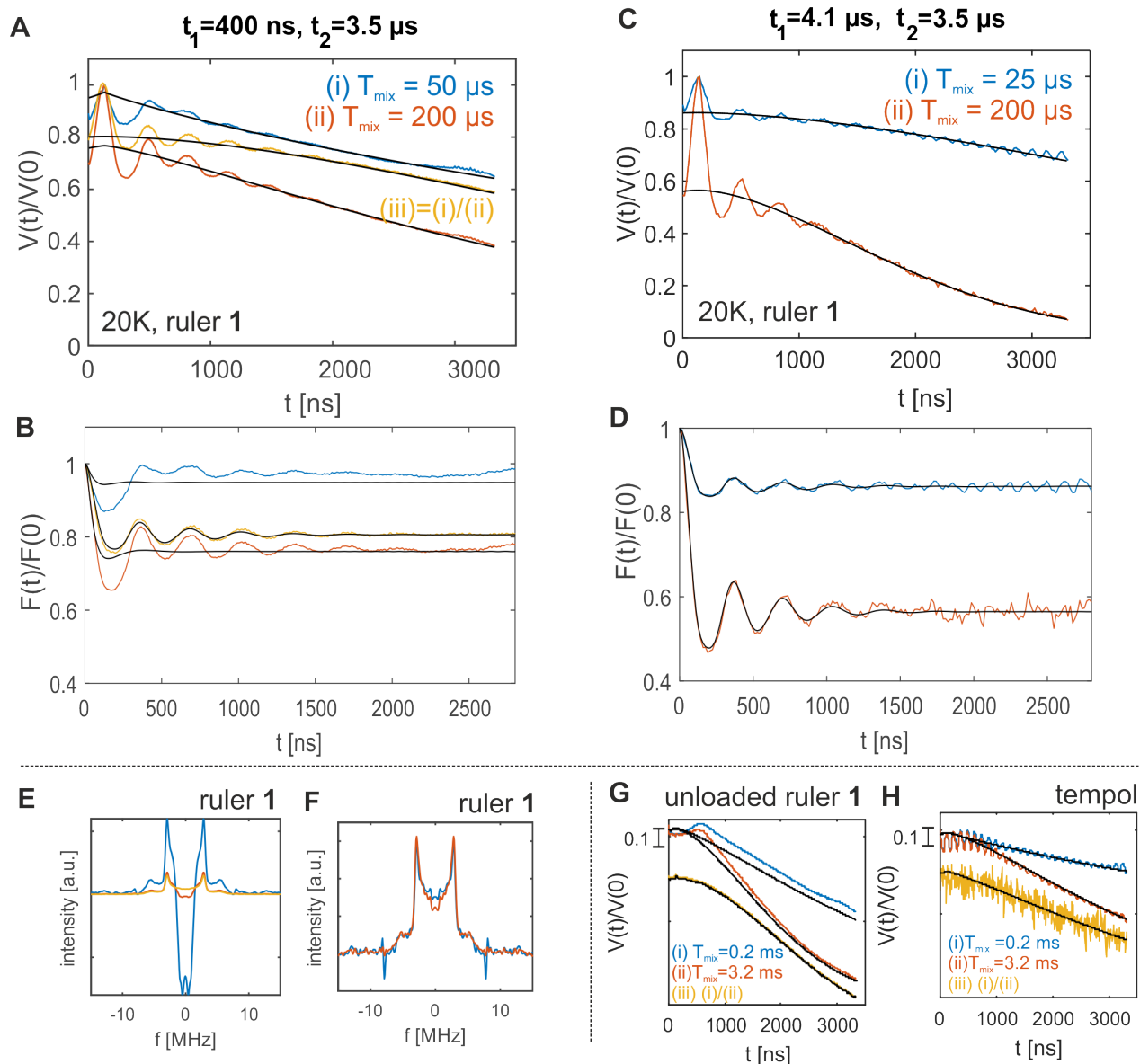
SI1 Fig. 29 Removal of background artifact including division approach; all data measured at 20 K with $t_2 = 3.5\,\mu s$; (A-F) ruler **1**; (A) normalised primary RIDME data with $t_1 = 0.4\,\mu s$ and (C) with $t_1 = 4.1\,\mu s$; mixing times are indicated in the legend. Blue traces correspond to the measurement at short T_{mix}, red traces at long T_{mix}, yellow traces are obtained by division of the complex signals after normalisation at the zero-time (to account for different signal intensities); (A,C) black traces are the background fit with a single stretched exponential function. Better fits can be obtained after division, or by measuring with long t_1. (B,D) Experimental form factors (colored), and fit (black) after background division; note that a longer T_{mix} than reported in the original study[34] is used for division. We observe good removal of the BG artifact, but a significant loss of modulation depth. (E) spectra of traces with $t_1 = 0.4\,\mu s$; (F) spectra of traces with $t_1 = 4.1\,\mu s$; (G) RIDME background measurement with unloaded ruler **1**, resp. (H) tempol; T_{mix} indicated in legend, yellow traces obtained by division, and shifted by 0.25 for visibility; background fit with single stretched exponential in black.

References

1 Y. Polyhach, E. Bordignon, R. Tschaggelar, S. Gandra, A. Godt and G. Jeschke, *Phys. Chem. Chem. Phys.*, 2012, **14**, 10762–10773.

2 R. Tschaggelar, B. Kasumaj, M. G. Santangelo, J. Forrer, P. Leger, H. Dube, F. Diederich, J. Harmer, R. Schuhmann, I. García-Rubio and G. Jeschke, *J. Magn.Reson.*, 2009, **200**, 81–87.

3 S. Stoll and A. Schweiger, *J. Magn. Reson.*, 2006, **178**, 42–55.

4 A. Savitsky, A. A. Dubinskii, M. Flores, W. Lubitz and K. Mobius, *The journal of physical chemistry. B*, 2007, **111**, 6245–6262.

5 B. E. Bode, J. Plackmeyer, T. F. Prisner and O. Schiemann, *The Journal of Physical Chemistry A*, 2008, **112**, 5064–5073.

6 A. Marko, D. Margraf, H. Yu, Y. Mu, G. Stock and T. Prisner, *The Journal of Chemical Physics*, 2009, **130**, 064102.

7 Y. Polyhach, A. Godt, C. Bauer and G. Jeschke, *Journal of Magnetic Resonance*, 2007, **185**, 118–129.

8 S. K. Misra, P. P. Borbat and J. H. Freed, *Appl. Magn. Reson.*, 2009, **36**, 237.

9 A. Marko, D. Margraf, P. Cekan, S. T. Sigurdsson, O. Schiemann and T. F. Prisner, *Physical Review E*, 2010, **81**, 021911.

10 C. Abé, D. Klose, F. Dietrich, W. H. Ziegler, Y. Polyhach, G. Jeschke and H.-J. Steinhoff, *Journal of Magnetic Resonance*, 2012, **216**, 53–61.

11 A. M. Bowen, C. E. Tait, C. R. Timmel and J. R. Harmer, *Structural Information from Spin-Labels and Intrinsic Paramagnetic Centres in the Biosciences*, Springer, Berlin, Heidelberg, 2013, pp. 283–327.

12 I. Kaminker, I. Tkach, N. Manukovsky, T. Huber, H. Yagi, G. Otting, M. Bennati and D. Goldfarb, *Journal of Magnetic Resonance*, 2013, **227**, 66–71.

13 A. Savitsky, J. Niklas, J. H. Golbeck, K. Mobius and W. Lubitz, *The journal of physical chemistry. B*, 2013, **117**, 11184–11199.

14 A. M.Bowen, M. W.Jones, J. E.Lovett, T. G.Gaule, M. J.McPherson, J. R.Dilworth, C. R.Timmel and J. R.Harmer, *Phys. Chem. Chem. Phys.*, 2016, **18**, 5981–5994.

15 A. Meyer, D. Abdullin, G. Schnakenburg and O. Schiemann, *Phys. Chem. Chem. Phys.*, 2016, **18**, 9262–9271.

16 A. M. Bowen, M. W. Jones, J. E. Lovett, T. G. Gaule, M. J. McPherson, J. R. Dilworth, C. R. Timmel and J. R. Harmer, *Phys. Chem. Chem. Phys.*, 2016, **18**, 5981–5994.

17 A. Giannoulis, C. L. Motion, M. Oranges, M. Bühl, G. M. Smith and B. E. Bode, *Phys. Chem. Chem. Phys.*, 2018, **20**, 2151–2154.

18 S. Milikisyants, F. Scarpelli, M. G. Finiguerra, M. Ubbink and M. Huber, *Journal of Magnetic Resonance*, 2009, **201**, 48–56.

19 P. P. Borbat and J. H. Freed, *Chemical Physics Letters*, 1999, **313**, 145–154.

20 G. Jeschke, M. Pannier, A. Godt and H. W. Spiess, *Chemical Physics Letters*, 2000, **331**, 243–252.

21 A. Godt, M. Schulte, H. Zimmermann and G. Jeschke, *Angewandte Chemie International Edition*, **45**, 7560–7564.

22 P. E. Spindler, Y. Zhang, B. Endeward, N. Gershernzon, T. E. Skinner, S. J. Glaser and T. F. Prisner, *Journal of Magnetic Resonance*, 2012, **218**, 49–58.

23 A. Doll and G. Jeschke, *J. Magn. Reson.*, 2017, **280**, 46–62.

24 P. Schöps, P. E. Spindler, A. Marko and T. F. Prisner, *Journal of Magnetic Resonance*, 2015, **250**, 55–62.

25 A. Doll, M. Qi, N. Wili, S. Pribitzer, A. Godt and G. Jeschke, *Journal of Magnetic Resonance*, 2015, **259**, 153–162.

26 A. Doll and G. Jeschke, *Phys. Chem. Chem. Phys.*, 2016, **18**, 23111–23120.

27 J. J. Jassoy, A. Meyer, S. Spicher, C. Wuebben and O. Schiemann, *Molecules (Basel, Switzerland)*, 2018, **23**, year.

28 R. Tschaggelar, F. D. Breitgoff, O. Oberhänsli, M. Qi, A. Godt and G. Jeschke, *Appl. Magn. Reson.*, 2017, **48**, 1273–1300.

29 I. Tkach, G. Sicoli, C. Höbartner and M. Bennati, *Journal of Magnetic Resonance*, 2011, **209**, 341–346.

30 A. Doll and G. Jeschke, *Journal of Magnetic Resonance*, 2014, **246**, 18–26.

31 G. Jeschke and Y. Polyhach, *Phys. Chem. Chem. Phys.*, 2007, **9**, 1895–1910.

32 C. Gemperle, G. Aebli, A. Schweiger and R. R. Ernst, *J. Magn. Reson.*, 1990, **88**, 241–256.

33 G. Jeschke, S. Pribitzer and A. Doll, *J. Phys. Chem. B*, 2015, **119**, 13570–13582.

34 D. Abdullin, F. Duthie, A. Meyer, E. S. Muller, G. Hagelueken and O. Schiemann, *The journal of physical chemistry. B*, 2015, **119**, 13534–13542.